ANL-7911
Reactor Technology

ARGONNE NATIONAL LABORATORY
9700 South Cass Avenue
Argonne, Illinois 60439

COMPARISON OF A TWO-DIMENSIONAL HYDRODYNAMICS CODE (REXCO) TO EXCURSION EXPERIMENTS FOR FAST REACTOR CONTAINMENT

by

J. E. Ash and R. T. Julke

Reactor Analysis and Safety Division

January 1972

DISCLAIMER

TABLE OF CONTENTS

LIST OF FIGURES

LIST OF FIGURES

LIST OF FIGURES

LIST OF TABLES

COMPARISON OF A TWO-DIMENSIONAL HYDRODYNAMICS CODE (REXCO) TO EXCURSION EXPERIMENTS FOR FAST REACTOR CONTAINMENT

by

J. E. Ash and R. T. Julke

ABSTRACT

The Reactor Excursion Containment Code System (REXCO) is a tool that has been developed at Argonne National Laboratory to predict the effects of excursions originating at the core upon the components and on the containment system of Liquid Metal Fast Breeder Reactors. The codes include hydrodynamic and inelastic material behavior depending on the magnitude of the excursion treated. The physical phenomena gaged by the codes involve the shock wave, the sodium momentum, and the early stages of the gas bubble. Current work attempts to extend treatment to the later, quasi-steady phenomena of the gas bubble.

In this report comparisons of these codes are made with experimental excursion data. The results of these comparisons confirm the capability of the REXCO code system to predict the response of the primary-system components and of containment structures to the generated pressure waves. The primary-system phenomena extend, but are not limited, to reactor-vessel strain and rupture, plug jump, and sodium escape past the cover seal into the secondary containment.

The validating comparisons were made with published experimental data. The subject experiments were conducted at A.W.R.E., Foulness, England; at Cadarache, France, by the CEA-Euratom and the UKAEA; and in the United States by the Naval Ordnance Laboratory.

I. INTRODUCTION

The REXCO-H code[1] is a time-dependent, hydrodynamic, two-spatial-dimension computer program designed to perform the numerical calculation describing the response of a primary reactor-containment system to a high-energy excursion. The hydrodynamic equations and the equations of state for the reactor materials are expressed in Lagrangian form. Cylindrical symmetry is assumed. Shock discontinuities are diffused by the introduction of an artificial viscosity. The code input, or initial values, are the pressures, internal energies, and velocities generated by the accident. Over the ensuing time the code computes the responsive displacements, velocities, pressures, specific internal energies, densities, and strains at finite time intervals. The computations are cyclically repeated for any number of time steps, or until a specified terminating condition, such as a vessel failure, is reached. The code has the capability of exhibiting graphically the pressure distributions, displacements, and motions, so that the shock-wave propagation, loading history and sequential damage to the reactor components can be traced throughout the course of the excursion.

The results obtained by use of a code of this nature provides information pertinent to the safe and economic design of reactor-containment systems. Given designs can be tested by computer runs to determine overall system integrity. It must be recognized, however, that all details of the response of a complex reactor system to a postulated accident cannot be computed exactly. In order for the computation to be manageable, even within the present advanced technology of large-scale computer systems, a number of simplifying assumptions must be made in the formulation of the problem. Only an approximation to the true solution can be expected by the computer run; if reliable measures of the degree of error can be determined, then factors of safety can be introduced to insure a desired level of safety. The effects of the introduction of any single given approximation can be determined accurately by analytical methods, but the cumulative effects of all the necessary approximations can only be estimated. Experimental evidence is required to establish the magnitudes of errors introduced by the required approximations and to verify the computer results.

In this report experimental results are compared with REXCO-H code computations. Four sets of experiments were analyzed. Each test case consisted of a model experiment in which the excursion energy release was simulated by the detonation of a chemical high-explosive charge. The results of the comparisons indicate that the REXCO-H code can be applied directly to certain containment problems involved in reactor safety. Not only can experimental data be reproduced with such a computer code, but through the use of the code as a research tool detailed insights can be gained into the relative effects of parameter variations. Optimal containment design for safety requires a wide range of quantitative measures of the relative performance of materials and structural configurations. Through the use of computer codes initial conditions can be varied easily to simulate possible accident situations, and the effects of design modifications can be assessed far more quickly and economically than by means of building and testing scale models.

II. REACTOR CONTAINMENT EXPERIMENTS

The REXCO-H code was designed to compute the loads imposed upon the structural components of a reactor-containment system for the time period immediately following a core explosion. To test the reliability of such computations, comparisons must be made with actual test data. For this purpose, a review was made of available test data, and four particular cases were selected as suitable for comparative studies. The first two test cases were performed by the U. K. Atomic Energy Authority (UKAEA). The first case is that of a bare, 2-oz RDX/TNT 60/40 charge in water. The second case involves the same charge enclosed within a simulated core and breeder structure. The third test case chosen for comparison is one of a series of sodium experiments carried out jointly by the CEA-Euratom and the UKAEA at Cadarache, France. The fourth test case is a U. S. Naval Ordnance Laboratory sodium experiment.

The experiments were selected on the basis of the simplicity of design and the appropriateness of the measured data for comparison with the REXCO-H code output. For consistency with the assumptions underlying the code, cylindrical symmetry in the experiments was a requirement. Also desirable in the experimental configuration were reasonably simple materials for which equation-of-state data are available. Since the code is a tool to achieve a balanced design for a safe and economical containment structure, the basic processes involved in a prototype accident should also occur in the experiments. The mechanisms included in the comparative studies are those that are dominant immediately following an explosion; these include plastic flow and rupture of metals, crushing of porous materials, shock-wave interactions, and the impulsive loading of shock-driven liquids.

Some of the available experiments are discussed briefly below.

A. The United Kingdom Atomic Energy Authority Experiments

Over the past decade, the UKAEA has conducted model studies for the containment of core explosions in fast reactor systems. In 1965, at a conference at Argonne National Laboratory, Rees[2] described a series of scaled model experiments in which core explosions were simulated by the detonation of small charges of chemical high explosives. These tests are particularly appropriate for comparison with the REXCO-H code results. The theoretical background for the tests was discussed by Hicks and Menzies,[2] who presented computations of the energy release and partitioning during an excursion and the concept of an equivalent chemical explosion. The simulation of the sequence of events following the core explosion by the detonation of a chemical detonation was discussed by Samuels.[2] The maximum hypothetical accident was assumed to be a super-prompt critical power excursion resulting from core compaction following a meltdown accident. The core is assumed to disintegrate with explosive violence, and the damage-producing mechanisms for the following few seconds are considered comparable to some equivalent TNT explosion. Although matching of the detailed time response of the structure cannot be expected, correlations of the broad effects are assumed. From the

model experiments, with appropriate scaling laws, the prototype peak pressures and the blast-wave impulse can be predicted. These gross results depend only upon the amount of energy released, its time scale, and the distance from the explosion. Close to the explosion, the effects depend upon the actual detonation process, but about 10 charge radii away (in water), the shock wave, which initially carries about 50% of the available energy, depends only upon the total amount of energy released. It is in this close region that significant irreversible heating takes place and about 25% of the detonation energy is deposited. The computation of these close-in effects may be important to the containment design because the early failure of some component close to the core may effectively channel the explosion energy and produce extremely high local stress concentrations. At distances beyond 10 charge radii further irreversible heating is small and the shock is approximately an acoustic wave. Analogous results can be expected in molten sodium, which has acoustic properties similar to those of water. The remaining roughly 50% of the detonation energy behind the shock wave is contained in the oscillating flow near the detonation gas cavity and is manifested in subsequent pressure pulses.

The question is yet open as to exactly how closely a chemical high explosive simulates a meltdown excursion. The excursion may be completed quickly enough (order of 1 msec) so that heat-transfer effects are negligible and peak pressures may reach 50 kb, compared to the peak pressure of about 100 kb for TNT. The heat energy remaining in the core materials may be 90% of that generated by the nuclear excursion, whereas for TNT almost all the detonation energy goes directly into mechanical compressive and kinetic energy. Hence, only about 10% of the nuclear energy should be simulated by the chemical explosive. The explosive effects of this 10% excess energy are assumed to be simulated by the chemical explosive for a time duration of the order of the first expansion of the explosive cavity. Beyond the first few seconds the concept of an equivalent explosive charge is no longer applicable.

It should be emphasized that the question of the validity of the modeling technique for the simulation of a nuclear excursion is to a large extent irrelevant to the comparison of the REXCO-H code with model tests. For the later application of the code to the hypothetical prototype nuclear excursion, it is only necessary that the code be verified in its ability to compute a similar sequence of events. Hence, as long as the model experiments reproduce the same kinds of events (i.e., shock loading, explosion cavity expansion, and subsequent pressure pulses, membrane rupture, impulsive loading, shock interaction compression, and rarefaction effects in heterogeneous media with differing acoustic impedances) the usefulness of the code as a tool for containment analysis can be established. Because of uncertain scaling laws, an experimental model may not establish a reliable basis for predicting prototype performance. But a code verified by means of such a model, and provided with the proper input conditions and equations of state, can be used with confidence to compute the expected prototype behavior.

On the basis of the available literature it appears that the bulk of the UKAEA small-scale model experiments involve high explosives in water. Certain tests were judged to be presently unsuitable for comparison with

the REXCO-H code either because the model configuration was too complex or because detailed pressure measurements were not made.

No attempt was made to compare the REXCO-H code with any large-scale accident data. Measurements suitable for direct comparison with the code are lacking. However, indirect comparisons could possibly be made. For example, for the SL-1 accident at Idaho Falls, analyses and interpretations are available* which may be utilized for comparative purposes.

The tests finally selected for comparison with the REXCO-H code are of a more simplified nature. As mentioned above, these are the tests described by Rees[2] for a 2-oz RDX/TNT charge in water. The detailed pressure measurements on the wall and roof of the 2-ft-dia, 2-ft-deep over-strong cylindrical containment vessel shown in Figs. 1 and 2, are especially useful for comparison with the basic computer code.

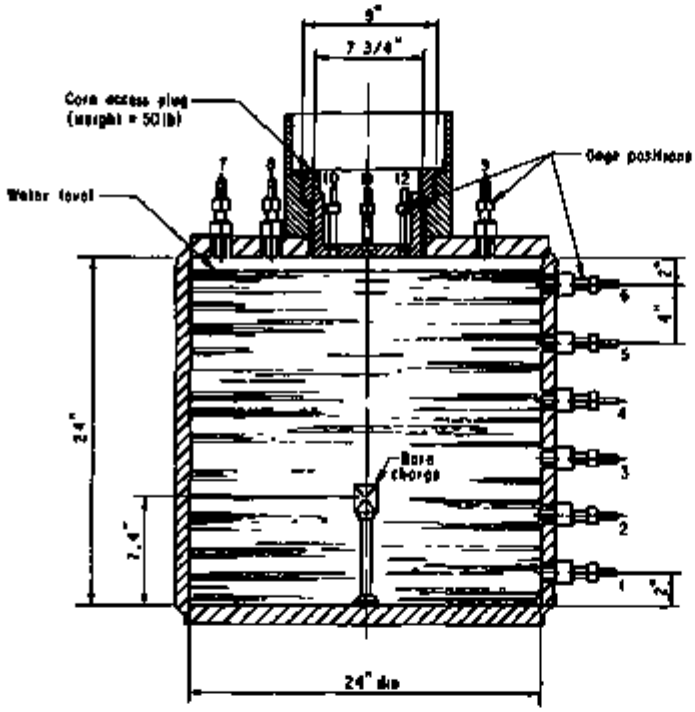

Fig. 1. Cross Section of Model Reactor Tank, Showing Positions of Pressure Gages and the Bare Charge [from "A Model Investigation of Explosion Containment in Single Tank Fast Reactors," by N. J. M. Rees (UKAEA), pp. 692-719, ANL-7120, Proc. Conf. on Safety, Fuels, and Core Design in Large Fast Power Reactors, at ANL, Oct. 11-14, 1965]. ANL Neg. No. 900-654.

B. Cadarache Experiments in Water and Hot Sodium Coolant

The interpretation of model experiments using water requires a knowledge of how the physical processes can be expected to differ if liquid sodium is the reactor coolant. There are also questions to be answered concerning the effects of using a cold liquid in the model to simulate the hot working fluid in the prototype reactor. An investigation into questions of this nature concerning model experiments was carried out jointly by the CEA-Euratom and the UKAEA at Cadarache, France.[3] The program consisted of a series of small-scale model tests using

* See *Hazard Summary Report on the ALPR*, ANL-5744.

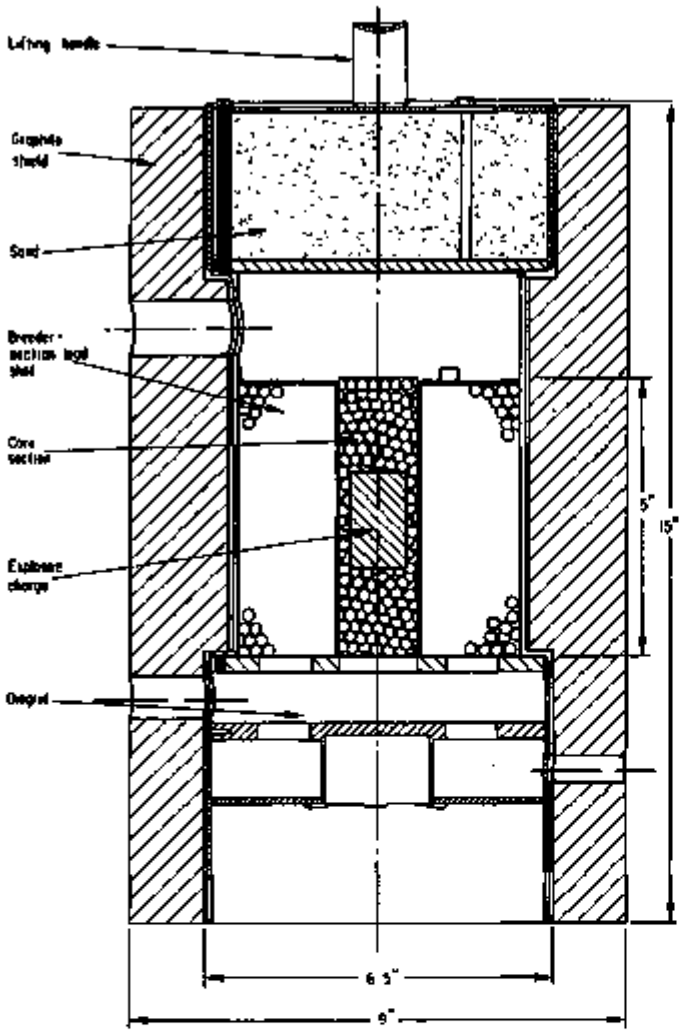

Fig. 2.
Cross Section of Model Core and Breeder Structure for UKAEA Experiments [from "A Model Investigation of Explosion Containment in Single Tank Fast Reactors," by N. J. M. Rees (UKAEA), pp. 692-719, ANL-7120, Proc. Conf. on Safety, Fuels, and Core Design in Large Fast Power Reactors, at ANL, Oct. 11-14, 1965]. ANL Neg. No. 900-673.

hexogene charges. The reported results of these tests appear to be appropriate for comparative studies with the REXCO-H code. The core vessel was simulated by a 25-cm-dia, 42.4-cm-deep, stainless steel tank (see Fig. 3). To study the relative scaling effects of different accident energy releases in the core, charge sizes of 15, 30, and 60 gm were detonated in both water and liquid sodium. For the 15- and 60-gm charges, the sodium tests were conducted at two contrasting temperatures: 150°C and 400°C; for the 30-gm charge, tests were made at four temperatures: 150, 250, 400, and 550°C. The variation in temperatures appeared to have no consistently significant effect within the scatter of the data. The pressure buildup in the argon gas cavity above the liquid, however, was somewhat higher for the hot liquid. To determine the impulse due to the blast pressure alone, the impulse from the sharply spiked pressure from the accelerated surface liquid thrown up by the shock wave was subtracted from the total impulse. Nothing was said about the temperature effect upon this impact pressure. If the particle velocity of the surface spray is v, then an approximation to the impact pressure can be calculated as ρcv, where c is the acoustic speed and ρ the liquid density. These calculated values were somewhat higher but yet comparable to the measured average impact pressure.

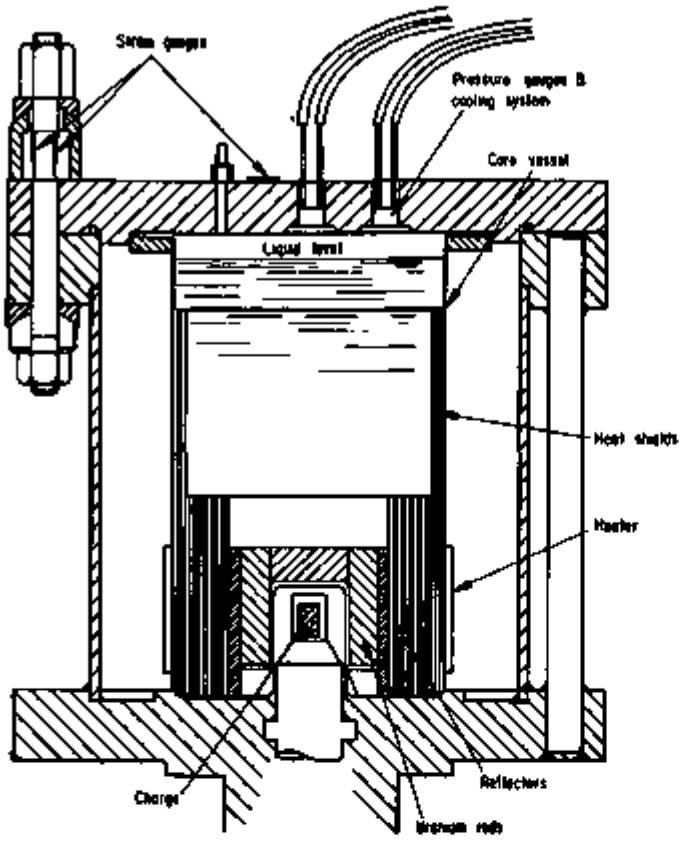

Fig. 3.
Main Components of the Model Reactor Assembly for the Cadarache Experiments [from "A Comparison of Pressure Loading Produced by Contained Explosions in Water and Sodium," by F. J. Walford (UKAEA), pp. 720-733, ANL-7120, Proc. Conf. on Safety, Fuels, and Core Design in Large Fast Power Reactors, at ANL, Oct. 11-14, 1965]. ANL Neg. No. 900-672.

Whereas the pressure appeared to be nearly independent of the liquid temperature, it was significantly dependent upon the type of liquid, that is, the pressure for the 15-gm charge was about 1.7 times as high in sodium as in water, and about 1.5 times as high for the 60-gm charge. The impulse can be assumed to consist of two parts. One part is associated with the impact of the surface liquid, and the other is attributed to the pressure of the compressed gas above the liquid surface. It was found that the impact impulse is independent of the type of liquid and can be approximated by $230W^{1/3}$ psi-ms, where W is the charge weight (gm) for both the sodium and the water. Thus, for one 30-gm charge, since the sodium pressure is higher than the water pressure by a factor of 1.5, the duration of the water-impact pulse is longer by a factor of 1.5 to produce the same impulse. To obtain a peak pressure in water equal to that in sodium the charge size should be doubled. However, since the pulse durations in the water are longer, the total impulse will be increased. Consequently, for the same peak pressures as in sodium, greater structural distortions will result in water experiments.

C. The Naval Ordnance Laboratory Experiments

During the period from the mid-1950's to the mid-1960's the United States Naval Ordnance Laboratory (NOL) conducted an experimental research program directed toward determining the response of a reactor vessel and containment system to a nuclear accident. Attention was focused on the Enrico Fermi Atomic Power Plant. A maximum hypothetical meltdown design accident was postulated as the equivalent of the detonation of 1000 lb TNT at the core location. A series of experiments to determine the

response of the shield plug, reported by Wise, Proctor, and Walker,[4] has been selected for comparison with the REXCO-H code.

It might be mentioned that during this same period, other experiments were being performed in the United States to study the response of model containment systems to simulated nuclear excursions. The Ballistic Research Laboratories ran tests to determine the response of models of steel containment buildings to internal loadings produced by detonating explosives. The Stanford Research Institute constructed model reactor vessels constrained by a radial concrete shield. The resulting fragment sizes and velocities were measured for loadings produced by mixtures of explosives and pyrotechnics.

In the NOL test program,[4] two distinctly different potentially destructive mechanisms were considered to be created by a detonating high explosive. The first is the shock wave assumed to contain initially about one-half of the released energy. The second is the "blast pressure" resulting from the expansion of the explosion gases, which initially contains the other half of the released energy. The shock-wave mechanism is very rapid, of the order of microseconds, and precedes the blast-pressure mechanism, which persists for milliseconds. The dominant cause of structural deformation and failure was claimed to be the impulse generated by the fluid momentum associated with the shock wave. The ensuing gas pressures were lower by an order of magnitude and insufficient to produce further significant vessel-wall deformation. Because of the inertia of the heavy shield plug, the shock-wave impulse may contribute only a small fraction of the plug-jump momentum. A significant plug jump depends upon the slower buildup of the blast pressure. The shock wave is still important indirectly to the plug jump, however, because failures of the primary shield due to the shock loading will greatly influence the resulting blast pressures.

Of concern to the containment designer is the fraction of released energy that is available for mechanical damage. For the experiments in cold water, about 10% of the high-explosive energy release went into the plug jump when the primary vessel ruptured. It is claimed that this percentage would be increased if the water were hot and decreased if the strains were smaller. Interpretation of the model test results with respect to the full-scale nuclear prototype is still open to question. It is not known exactly what percentage of the accident energy release is promptly transferred to the coolant. If 10% is available, then only 1% of the total release will be expected for mechanical damage. For the SL-1 accident the prompt and total energy releases were estimated to be 50 and 130 MW-sec. But the reactor was cold, and this ratio can be expected to be considerably reduced under normal higher-temperature operating conditions.

Because the principal objective of the NOL experiments was the response of the shield plug to a postulated nuclear excursion, detailed measurements of the shock-wave pressures were not made. Rather, only the blast pressures were measured in the experimental configuration shown in Fig. 4. Consequently, a detailed comparison of the REXCO-H computations with the test results cannot be achieved. Nevertheless,

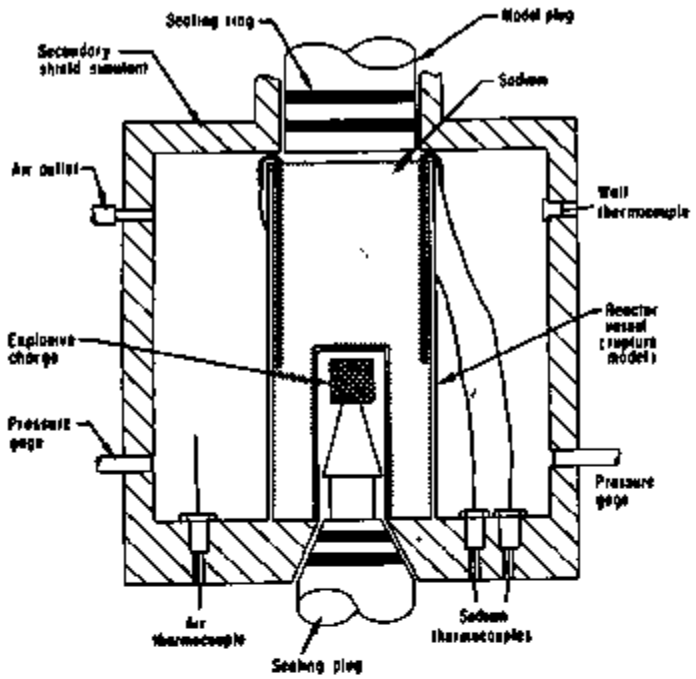

Fig. 4.
Rupture Model Assembled in Idealization of Model Secondary Shield for Naval Ordnance Laboratory Experiments [from "Response of Enrico Fermi Reactor to TNT Simulated Nuclear Accidents", p. 29, NOLTR 62-207, November 1964]. ANL Neg. No. 900-671.

the NOL tests appear to provide the most suitable data in the United States for comparative purposes. The comparisons obtained are significant and informative and are discussed in Sect. III.

III. COMPARISON OF THE REXCO-H CODE WITH EXPERIMENTS

The REXCO-H code generates the numerical solution to a set of finite-difference equations representing a system of differential equations. The system of differential equations, together with equations of state for the constituent materials, is the mathematical model of the physical system. How closely the numerical solution approximates the true solution of the differential equations, depends upon a number of considerations involving the stability and convergence of the numerical techniques. Some of these considerations are discussed in Appendix A. The point is made that in a numerical analysis certain questions cannot be resolved completely by analytical means alone. To test the overall reliability of the code performance, comparisons must be made with experimental results. Possible discrepancies between code results and experimental data do not necessarily imply poor performance of the code in obtaining numerical solutions to the mathematical model. The mathematical model itself, which is an idealization of the actual physical system, may be inadequate. The accurate range of an equation of state may be too narrow or certain processes may be incorrectly hypothesized. For this reason, the experiments chosen for comparison should conform as nearly as possible to the idealized mathematical model.

The four sets of model experiments chosen for comparison, described in Sect. II, range in complexity from the very simple bare charge in water to a relatively complex configuration of simulated blankets and shields in sodium. The first and most clear-cut experiment is the bare explosive charge suspended in a small rigid tank containing water. In this experiment the discrepancies between the mathematical model and the actual physical events are expected to be minimized. The equations of state for the water and the explosive are reasonably well-known and ought not to be a major source of error. Since the charge volume is small compared to that of the tank, the effects of deviations from the hypothesized detonation process and nonsymmetries in the vicinity of the charge should be negligible. Hence, in terms of checking the computational performance of the code, this first test should be most important. The results of the comparison with this test and three subsequent experiments, are discussed in detail below.

A. The Bare Charge in Water

The experiments conducted by UKAEA for the bare charge in water are reported by Rees.[2] A 2-oz (56.7-gm) charge of RDX/TNT 60/40 was suspended in water contained in the rigid vessel shown in Fig. 1. The pressures were measured at the tank wall and roof with piezoelectric transducers. The natural resonance of the gauge was specified as 300 kHz, the length as 0.88 in., diameter as 0.44 in.; the diameter of the quartz crystal was 0.25 in. and its thickness 0.125 in. The gauge output was 0.5 pC/psi, and the system frequency response ranges from 0 to 20 kHz. It should be noted that these experiments were run before 1965; a much faster response (of the order of 40 kHz) can be attained with currently available systems. For a very sharp rise and decay of the shock incident upon the tank wall, the peak pressure will be cut off and the recorded pressure peak will be less than the actual peak. The instrumentation was

not capable of following a very sharply peaked pressure pulse; as a result the recorded pressure peak for an accident shock at the wall was expected to be less than the actual peak.

The data described by Rees was analyzed by Hoskin[7] and compared with computer code calculations. The code used by Hoskin is apparently similar to REXCO-H. It, too, is an unsteady, two-dimensional (cylindrical symmetry) Lagrangian code in which shocks are smeared by pseudo-viscous terms. Hoskin concludes that the comparisons demonstrate that through the use of high-speed computers "accurate estimates of pressure loadings can be made for experiments involving explosive charges."

The equations of state for both the water and the explosive source are reasonably well established. The equation of state for the explosive is discussed in Appendix B. The forms given by both Amsden and Hoskin were used in the REXCO-H code, and the differences in the end result (i.e., the pressures computed at the tank wall) were found not to be significant. Also, two different equations of state for water were used; again, the end results did not appear to differ significantly. The first equation of state for water was based upon a Hugoniot curve taken from Ref. 9. State points off the Hugoniot curve were described by a Mie-Grüneisen form with $\Gamma = 1.32$:

$$p = p_H + \Gamma\rho(e - e_H) \quad . \tag{1}$$

The computed (p,v) state histories for particles at several positions, along the cylindrical radial line through the explosive center, is shown in Fig. 5.

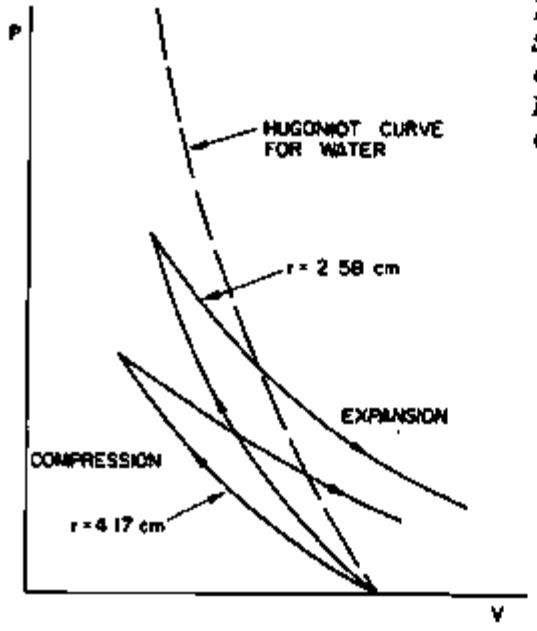

Fig. 5.
Schematic (p,v) State Paths for Shock Compression and Expansion at Two Radial Positions at the Charge Elevation (Bare Charge in Water).

The second equation of state used for water was that given by Hoskin:

$$p = \rho_o(A + Be) \qquad (\text{dyne/cm}^2), \tag{2}$$

where

$$A = \mu(2.56 + 2.8867\ \mu)10^{10};\ B = 2.552 + 1.6491\ \mu;$$

$$\mu = (\rho/\rho_o) - 1\ .$$

The value for the initial water density ρ_o was taken to be 1.0 gm/cm^3. Equation 2 was obtained by a straight-line fit to the Hugoniot data of Rice and Walsh[8] for the shock and particle speeds:

$$U = a + bu_p\ . \tag{3}$$

For a least-squares fit at 5 and 200 kb the coefficients are

$$a = 1.6(10^5)\ \text{cm/sec};\ b = 1.6276$$

The form of Eq. 2 is derived by combining the Hugoniot fit with the Rankin-Hugoniot relations for conservation of mass, momentum, and energy:

$$\text{mass:}\quad u_p = \frac{\mu}{\mu + 1}\,U;$$

$$\text{momentum:}\quad p_H = \rho_o U u_p;$$

$$\text{energy:}\quad p_H\,u_p = \rho_o\,U[(u_p^2/2) + e_H]\ .$$

From the Rankin-Hugoniot relations,

$$e_H = u_p^2/2;\ p_H = \rho_o(a + bu_p)u_p\ .$$

The particle velocity is

$$u_p = a\mu/[1 - (b - 1)\mu]\ ,$$

and, neglecting terms of order $0(\mu^3)$, the binomial expansion gives

$$u_p \approx a\mu[1 + (b - 1)\mu];\ u_p^2 \approx a^2\mu^2\ .$$

Substitution into the Mie-Grüneisen form Eq. 1, letting $\Gamma = 2b - 1 = 2.2552$, gives* the coefficients in Eq. 2:

$$A = \mu(a^2 + a^2 \frac{\Gamma}{2} \mu); \quad B = \Gamma + \Gamma\mu.$$

For each cell the values of p and e are computed from the simultaneous solution of the equation of state and the energy equation (primed quantities are known values from the previous time cycle):

$$\Delta e = -\frac{1}{2} (P' + p)\Delta v \ , \tag{4}$$

where

$$\Delta e = e - e'; \ \Delta v = v - v'; \ P = p + q \ .$$

From Eq. 2 the explicit solution for the internal energy is

$$e = [e' - \frac{1}{2} (P' + A)\Delta v]/(1 + \frac{1}{2} B \Delta v) \ . \tag{5}$$

Negative values of p are not permitted since water cannot sustain any significant tension; if the solution of Eqs. 2 and 5 gives a negative pressure, then p is set equal to zero and e is calculated directly from Eq. 4.

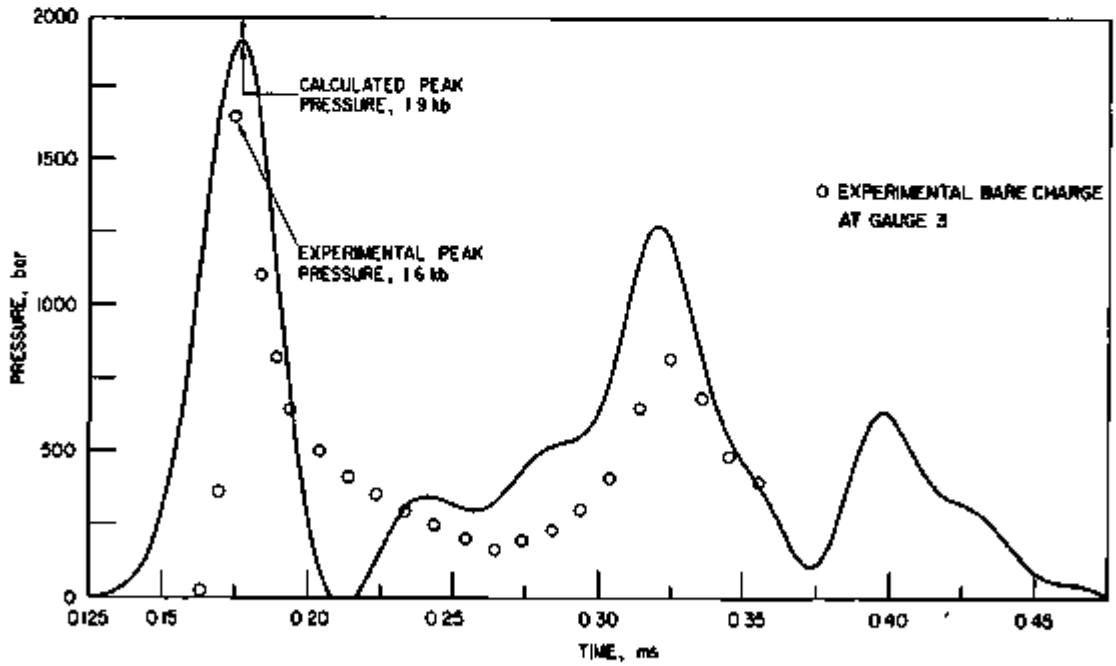

Fig. 6. Comparison of REXCO-H Computed Pressures with Measured Values at Gauge-3 Position (Bare Charge in Water)

* Note that in the second term for B, the coefficient used by Hoskin is 1.6491 rather than Γ. To compare our code results we used his value.

In Fig. 6 the REXCO-H computed pressures on the tank wall at the gauge-3 position are compared with the measured values. The computed peak shock pressure is 27,700 psi, about 20% greater than the measured value of 23,100 psi. This discrepancy is to be expected in view of the instrument lag; the peak pressure is cut off because the measuring-system response is not sufficiently fast to follow the sharply peaked shock. For this computation the equations of state used for the water and explosive were those given by Hoskin. The cylindrically shaped explosive was permitted to burn radially outward at a constant burn rate of 7991 m/sec (see Appendix B). The advance of the shock wave radially outward toward the wall, and the corresponding grid deformation, is shown in Fig. 7.

The initial advance of the shock wave should remain symmetrical about the charge center until interference effects from the bottom reflection become significant. Actually, for the cylindrical coordinate system used, the cell volumes increased radially outward from the cylindrical axis. Hence, the numerical grid was not spherically symmetric; as a consequence, numerical deviations from spherical symmetry were induced, even when the actual phenomena were perfectly symmetric about the charge center. Comparison of a radial and axial computed pressure profile is shown in Fig. 8.

The plotted pressure profiles of the computer output shown in Fig. 7 are to a linear scale and show the major pressure pulses; however, the details of the smaller pressures do not show up very well. The pressures should be plotted to a logarithmic scale, as shown in Fig. 9. To obtain more detail in the computation a fine grid was used, and in place of the two cells for the half-space containing the explosive shown in Fig. 7, the explosive was partitioned into 26 cells, or 13 cells for the quadrant shown in Fig. 10.

For the computation of the pressure profiles shown in Fig. 9, the grid was repeatedly rezoned. The maximum grid distortion was confined to values from 5 to 8. For example, the grid distortion shortly following the detonation is shown in Fig. 10. The distortion is confined to the explosive-water interface. If a smooth curve were used here, the distortion would be reduced. The pressure profile at $t = 56.35$ μsec shows an oscillating wave train developing behind the shock front. When the grid was coarsened at this point (grid size doubled) the finer details of the wave structure were lost, and a smoother wave profile was obtained for $t = 112.25$ μsec, just prior to incidence at the wall. When the fine grid structure was maintained until the shock front reached the wall, the peak was sharper and the peak reflected pressure was higher, 2.5 kb compared to 2.0 kb for the coarser grid. These pressure values are along the radial line through the charge, where the incident shock pressure is normal to the wall. The peak pressures at the gauge-3 position were reduced because the wave was oblique to the gauge face and more distant from the shock center.

At the gauge-3 position the incident shock was obliquely inclined to the wall; the shock was normal to the wall 2.6 in. below gauge 3, directly opposite the charge center. In Fig. 11 the computed pressure traces at

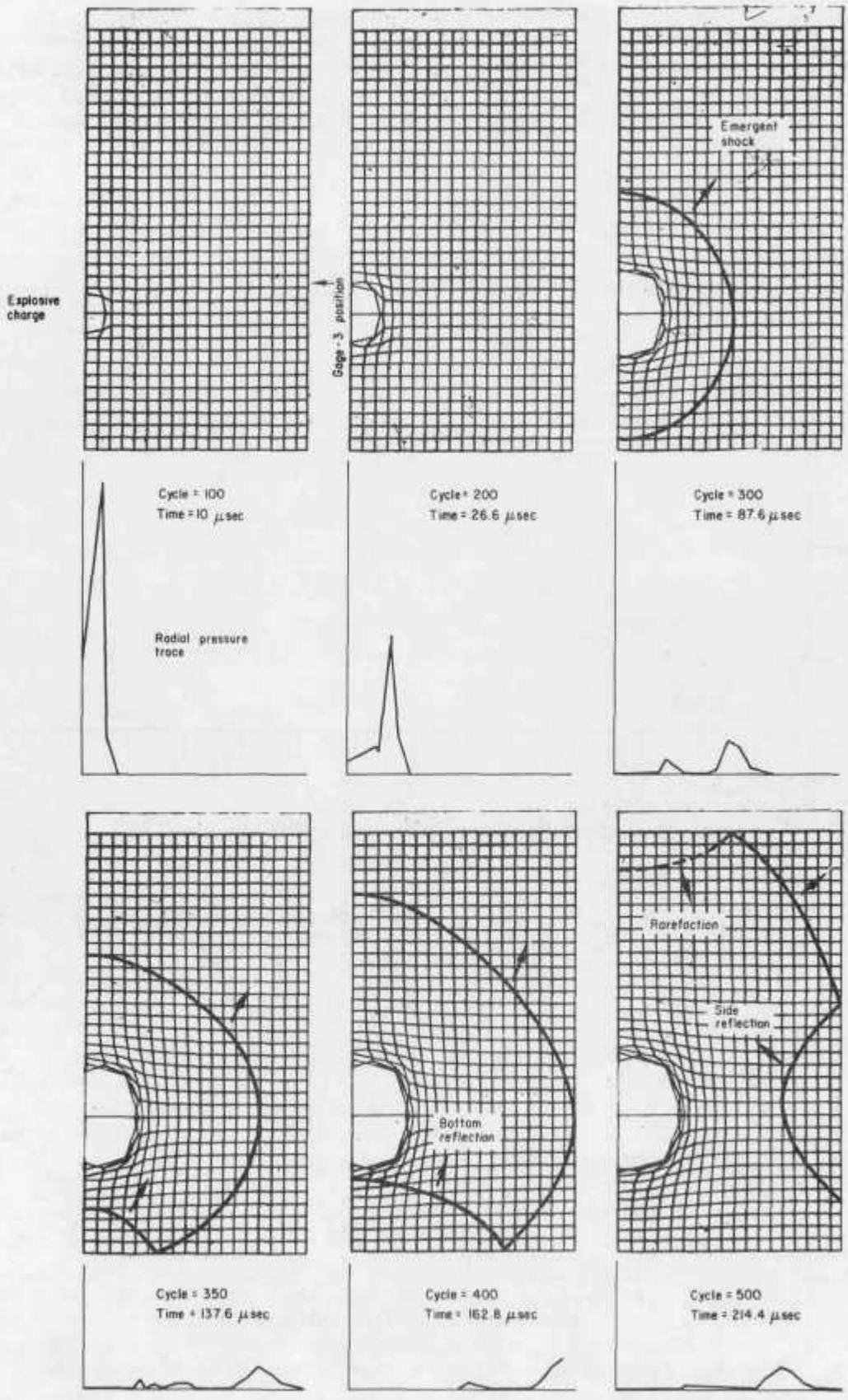

Fig. 7. Progressive Pressure Wave Advancing Radially Outward from the Bare Charge, and Corresponding Grid Distortion

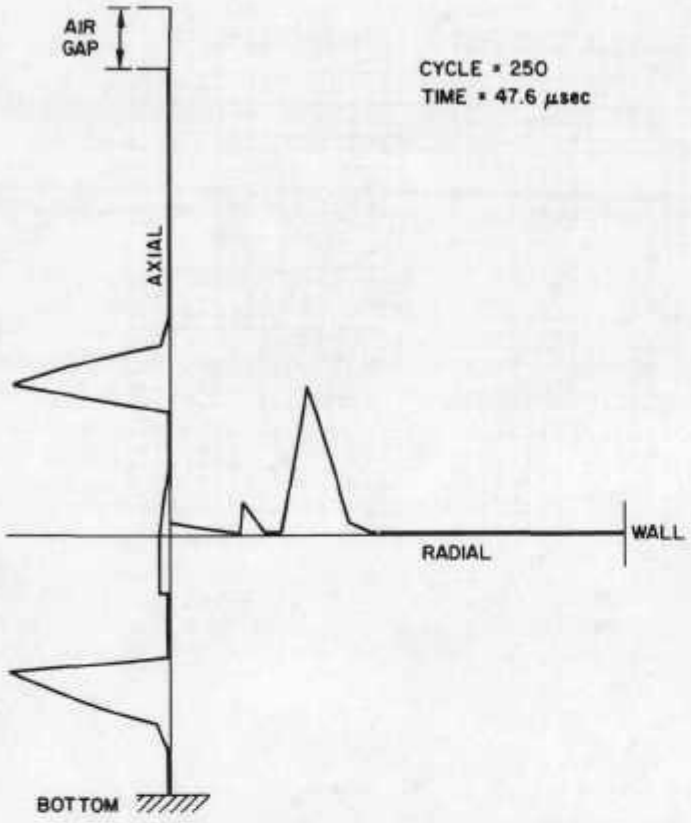

Fig. 8. Comparison of Pressure Profiles Along Cylindrical Axis and Along Radial Line through Explosive Center

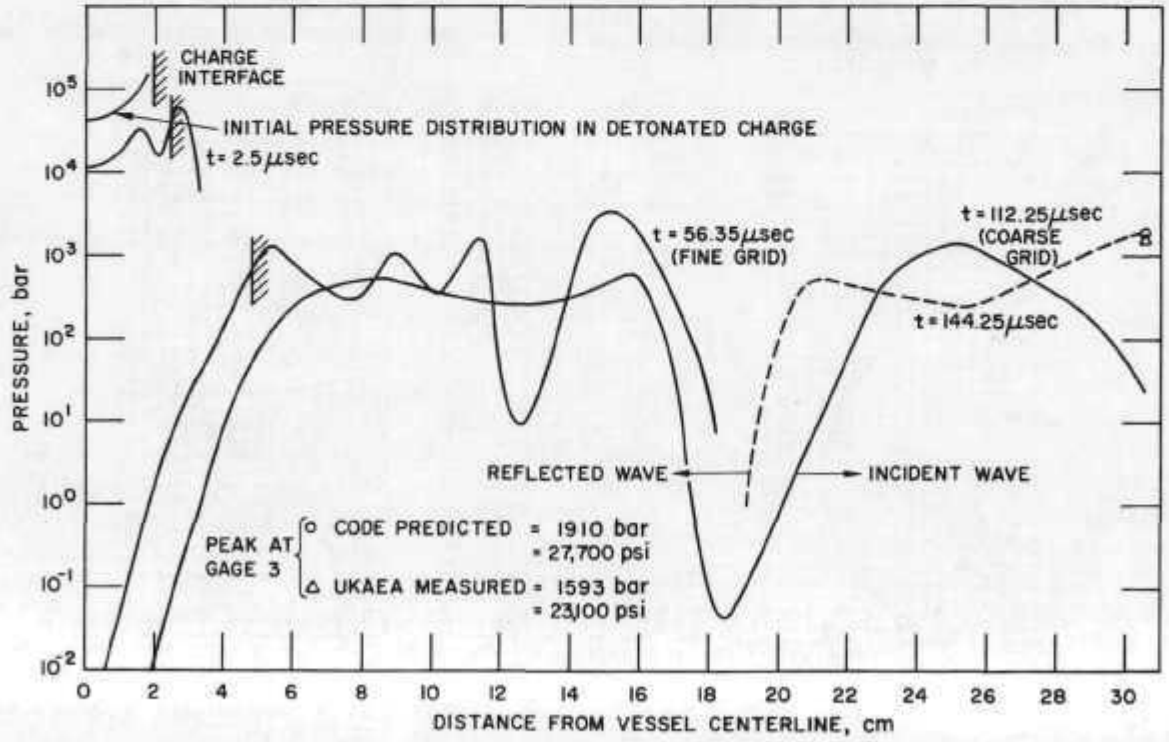

Fig. 9. Computed Pressure Profiles in the Radial Direction as the Shock Wave Advances toward the Wall (Bare RDX/TNT Charge in Water)

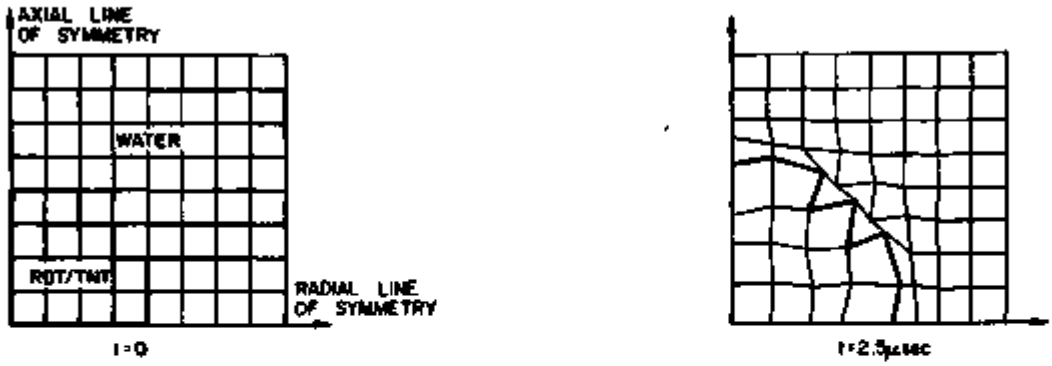

Fig. 10. Grid Distortion for Fine Grid at Point of Reasoning

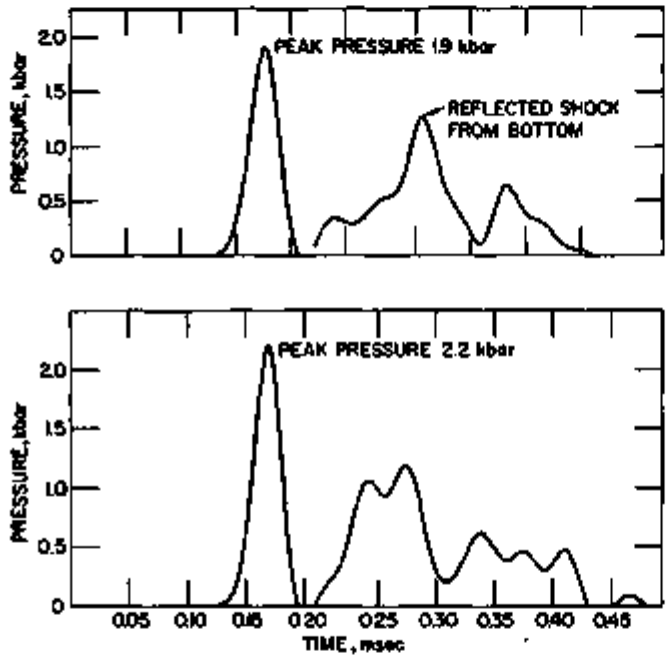

Fig. 11. Comparison of the Pressure Trace at Gauge 3 (Oblique Incidence) with the Trace at the Wall Opposite the Charge (Normal Incidence)

these two points are compared. The peak pressure for the normal shock was 31,900 psi, considerably higher than the 27,700-psi peak at gauge 3. The incident shock arrived somewhat earlier because the radial distance from the charge to the wall was a little less, and the reflected shock from the bottom was significantly earlier. It may be noticed that the reflected shock was beginning to blend with another pressure pulse. This other pressure pulse is the second pulse emerging from the charge, more clearly seen in Fig. 9. By the time this second pulse reached gauge 3, it was already obscured by the combined actions of the rarefaction following the first pulse and the bottom-reflected shock. The subsequent pulses represented more complex interactions, and individual components were difficult to distinguish.

At the tank top the computed pressure within the trapped air space gradually increased as the water surface rose as shown in Fig. 12. The computed peak pressure was 0.83 kb or 12,035 psi. This computed pressure compares with the measured pressure of 12,500 psi by gauge 12 in the core access plug.

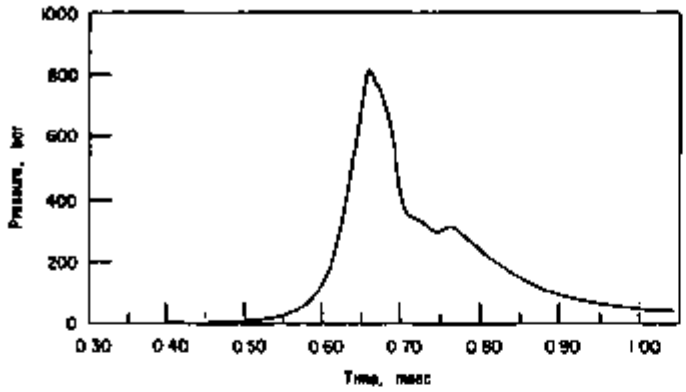

Fig. 12.
The Computed Pressure History in the Trapped Air Space above the Liquid Surface (Bare Charge). ANL Neg. No. 900-676.

The total energy should be conserved throughout the computational process. Some deviations are to be expected from the natural errors introduced by the finite-difference approximations (see Appendix A, Sect. 2), and to a minor extent by small round-off errors. The most substantial deviations from energy conservation are caused by the grid distortion which develops if the computation is not frequently rezoned. Trial computations have indicated, however, that these distortions have little effect upon the early shock pressures at the tank walls or upon the early motion of the free liquid surface. Consequently, the computation was permitted to proceed, without introducing the disturbances caused by rezoning, to calculate the pressure loadings at the walls and roof. While the accuracy of these computed pressure loadings were maintained, the internal distortions caused deviations from an invariant total energy to grow as shown in Table 1.

B. The Charge Enclosed in a Core and Breeder Structure

The second test case selected for comparison with the REXCO-H code was also performed by the UKAEA, and involved the same bare charge and containment-tank configuration discussed above, but the charge was confined in the structure shown in Fig. 2. In the experiment, the effect of the enclosing structure was to delay the time of arrival of the pressure wave reaching the wall and to smear out the wave form significantly. The sharp peak observed for the bare charge was completely suppressed, as shown by Hoskin (see Fig. D1 in Appendix D); the pressure developed more gradually to a peak of 3,480 psi, or 0.24 kb, at gauge 3, compared to the peak shock pressure of 23,100 psi, or 1.59 kb, for the bare charge. Thus, the measured effect of the structure is to reduce the peak pressure reaching the containment wall (at gauge 3) by a factor of about six. The pressure computed by REXCO-H was 0.60 kb, so the effect of the confining structure is to attentuate the computed peak pressure at the gauge-3 position by a factor of only three.

Since the performance of the REXCO-H code, in terms of its ability to perform the essential numerical computations, is reasonably well-established by its comparison with the bare-charge experiment, it would appear that the source of error lies in the equations of state of the materials. Particularly unreliable is the description of the lead shot. The lead shot was treated in three different ways. First, the lead shot was assumed to be water saturated (that is, the interstices between the

Table I. Energy Balance (for Bare Charge in Water) Calculated by REXCO-H Code

Time, μsec	Computational Cycle	Internal Energy, kW-sec	Kinetic Energy, kW-sec	Total Energy, kW-sec	Deviation of Energy, %
0	0	-	-	-	-
0.5	5	44.69	0.0004	44.69	-
1.0	10	192.93	0.0365	192.97	-
1.5	15	446.71	0.457	447.17	-
2.0	20	804.68	2.651	807.33	-
2.3[a]	23	1016.8	6.143	1023.0	-
5.0	50	945.45	78.36	1023.8	0.07
10.0	100	891.44	134.23	1025.7	0.26
26.6	200	895.42	156.97	1052.4	2.87
87.6	300	901.89	152.96	1054.8	3.11
162.8	400	923.11	131.22	1054.3	3.06
214.4	500	959.35	95.37	1054.7	3.10
329.6	600	939.27	117.89	1057.2	3.34
394.0	700	899.79	158.55	1058.3	3.45
474.0	800	883.84	175.36	1054.2	3.54
610.8	900	900.21	157.68	1057.9	3.41
770.8	1000	953.66	85.59	1039.3	1.59
866.2	1100	971.26	57.71	1029.0	0.59
973.4	1200	979.36	45.43	1024.8	0.18
1047.0	1300	982.56	39.80	1022.4	0.06

[a] End of burning (56.7-gm cylindrical charge; h = 3.51 cm; r = 1.755 cm; constant burn velocity = 7991 m/sec; specific energy release = 4.789 kW-sec/gm).

shot were permeated with water) and a Hugoniot curve was constructed* for a mixture of 35% water and 65% lead by volume. All materials were treated hydrodynamically, in the sense that shear stresses were neglected, and as a result the energy absorption of the confining structure was unrealistically low. The effect of the confining structure was to alter the pressure profile, as may be observed by comparing Fig. 13 with Fig. 9 for the bare charge. The net attenuation of the peak pressure at the gauge-3 position was not significant. Subsequent communication with the UKAEA revealed that the lead shot was not water saturated and should be treated as a truly porous material rather than as a liquid-solid mixture.

The equation of state was modified to permit the absorption of energy by the crushing of the voids between the lead shot as described in Appendix D. As a result, the peak pressure was attenuated to a value of 1.1 kb, approximately one-half of the previous peak for the water-filled voids. This attenuation, however, was insufficient when compared

* See Ref. 1, Appendix B, "Equation of State for a Group of Mixed Materials."

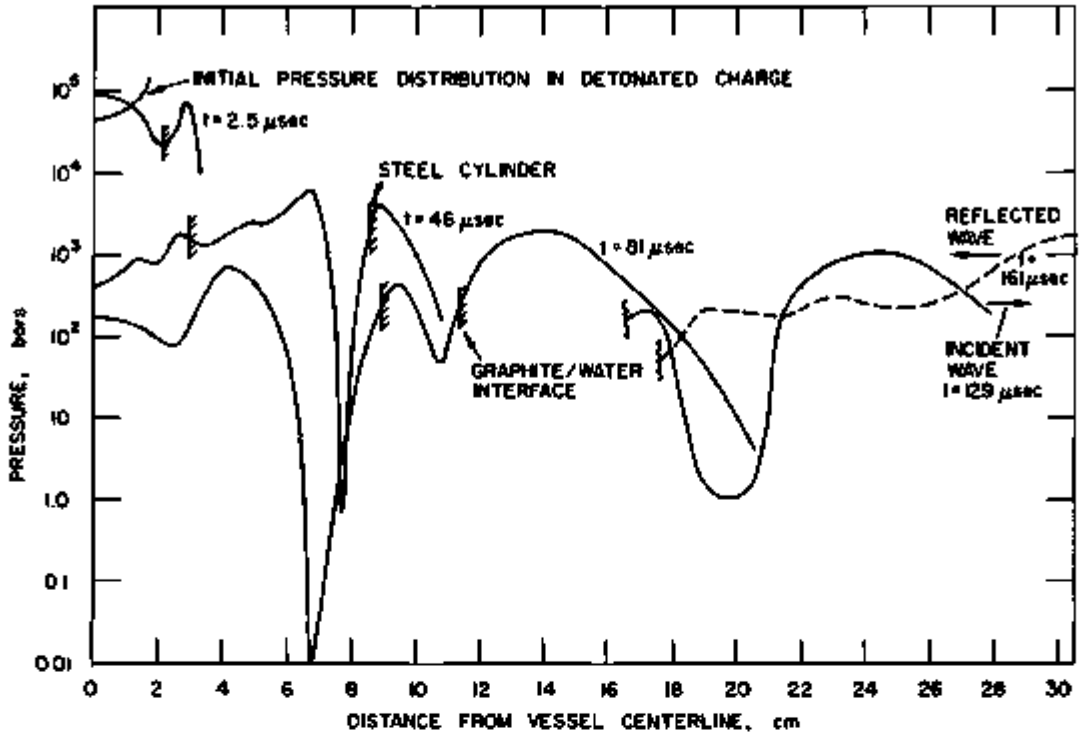

Fig. 13. Computed Radial Hydrodynamic Pressure Profile for the Confined Charge (Water-saturated Lead Shot)

to the experimental performance of the confining structure. Shear stresses were neglected in the hydrodynamic equations for the lead shot. Since the pressure pulse reaching the wall is not sharply peaked, and the peak itself is considerably smaller than the value for the bare charge, the mechanical effects at the lower pressures become dominant. The neglect of the shear stresses in proportion to the hydrostatic pressure at the lower pressures will lead to significant error.

For a more realistic description of the attenuation process, the energy absorbed by the shear stresses must be computed. In the third trial computation, the elastic-plastic equations described in Appendix A, Sect. 5 were applied to the compacted lead shot. These computations were performed with the inelastic code supplement.[6] The additional mechanical energy dissipated by the shear stresses produced an attenuation of the peak pressure down to a value of 0.60 kb; the computed pressure history at the gauge-3 position is shown in Fig. 14. This peak value is not as low as the measured peak value of 0.24 kb, but it is fairly clear that the discrepancy is due to the inaccurate description of the lead shot, rather than to deficiencies in the basic REXCO-H code. The supplementary inelastic code treats the lead-shot region as if it were a homogeneous, isotropic medium of compacted lead, i.e., essentially as if the lead-shot region were a thick-walled lead cylinder. Actually, the material structure is quite different; before the shot is compacted the material is obviously not isotropic, and remains so throughout its elastic range. From the computation it was found that a significant portion, about one-third, of the shot had not been completely compacted. The distorted configuration

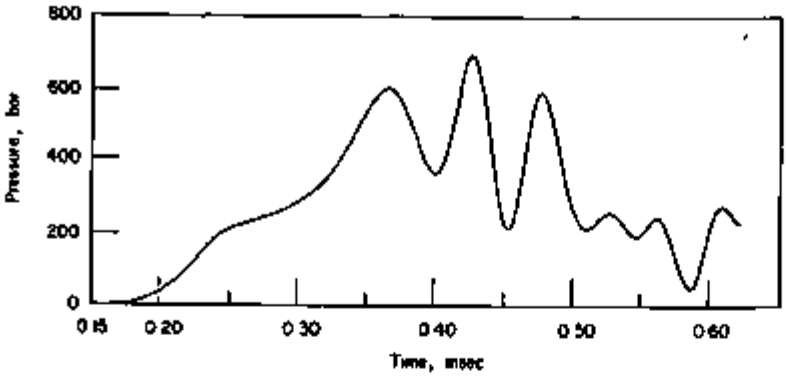

Fig. 14. The Computed Pressure Trace at the Gauge-3 Position for the Confined Charge. ANL Neg. No. 900-678.

at the time of the 0.6-kb pressure peak is shown in Fig. 15. To obtain a better correlation with the experiments, an improvement in the inelastic code is needed, specifically to treat a nonisotropic material.

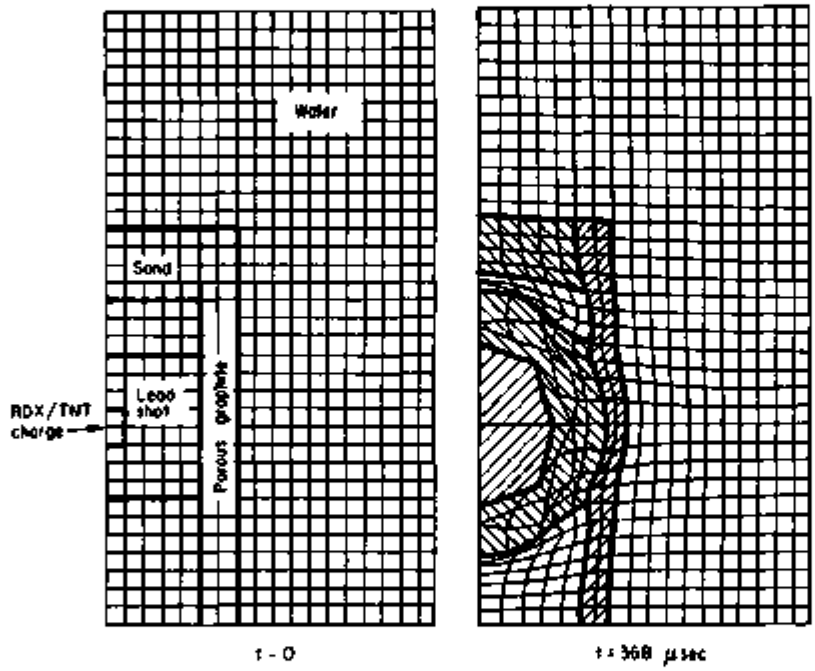

Fig. 15. Configuration of Confined Charge at Initial Time Compared with Distortion at Time of Peak Pressure at Gauge-3 Position. ANL Neg. No. 900-806.

C. The Cadarache Experiments in Sodium

The third test case chosen for comparison is from a series of scale-model experiments carried out jointly by the CEA-Euratom and the UKAEA at Cadarache, France. The experimental configuration is shown in Fig. 3. Hexogene charges (15, 30, and 60 gm) were introduced into a 25-cm-diameter, 42.4-cm-high, steel, simulated core vessel. The blankets were simulated by a mixture of uranium and steel rods (average density of 12.7 gm/cm^3); the neutron reflectors were represented by six concentric stainless steel cylinders, 0.25 cm thick, spaced 0.1 cm apart; the heat shield was represented by four longer, 0.1-cm-thick cylinders, spaced 0.1 cm apart. Experimental data were obtained for the three charge weights in both water and sodium.

For comparative purposes more instrumentation would have been desirable in the experiments; in particular, at least one pressure probe should have been immersed in the liquid for the direct measurement of the shock strength.

The pressure gauges located in the top plate first recorded the initial gradual buildup of pressure in the air space above the sodium free surface. Then the liquid sodium impinged directly upon the gauge face, causing a rapid rise in the pressure. This pressure surge extended over a period of the order of 0.2 msec. The recorded pressure traces show an ill-defined noisy hash during this period, with peaks at 17,000 to 19,000 psi. At the completion of the surge, at about 1.2 msec, the liquid sodium had apparently receded, and the initial gradual pressure buildup in the air space resumed.

It is apparent that the response of the instrumentation system was not sufficiently fast to record the details of the rapidly fluctuating pressure generated when the liquid sodium strikes the top plate. The computed pressure fluctuations are shown in Fig. 16. The first pressure

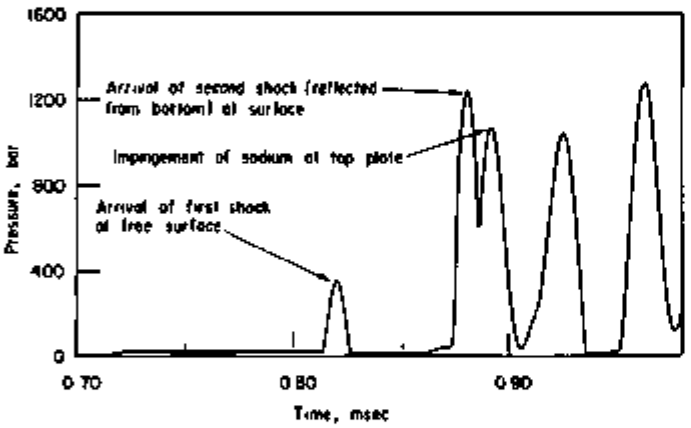

Fig. 16.
The REXCO-H Computed Pressure Trace at the Sodium Free Surface and at the Top Plate after Slug Impingement for the Cadarache Experiment (60-gm Hexogene Charge). ANL Neg. No. 900-680.

pulse arrived at the free surface at 0.82 msec and is not sensed at the gauge in the top plate. A second shock pressure, probably a reflection from the bottom, arrives at the sodium surface at 0.885 msec, and at 0.890 msec the sodium surface impinges upon the top plate. The pressure immediately rises again, followed by alternate rarefactions and pressure surges. The computed pressure peaks are in the neighborhood of 18,000 psi, compared to the experimentally measured peaks of 17,210 psi and 19,250 psi for sodium at 150 and 400°C, respectively. The reported standard error is 1,250 psi, so it may be concluded that the REXCO-H computed peak pressure is in agreement, within experimental error, with the measured peak pressure in the Cadarache sodium experiments.

The computation was stopped after 1 msec because of excessive cell distortion. Actually, as may be observed in the sequence of Figs. 17 and 18, cell distortion in the central region becomes excessive much earlier, so that the inner mesh is grossly distorted throughout almost all of the computation. However, the cells in the region of the liquid surface remain relatively undistorted up to 1 msec, and the pressures in this

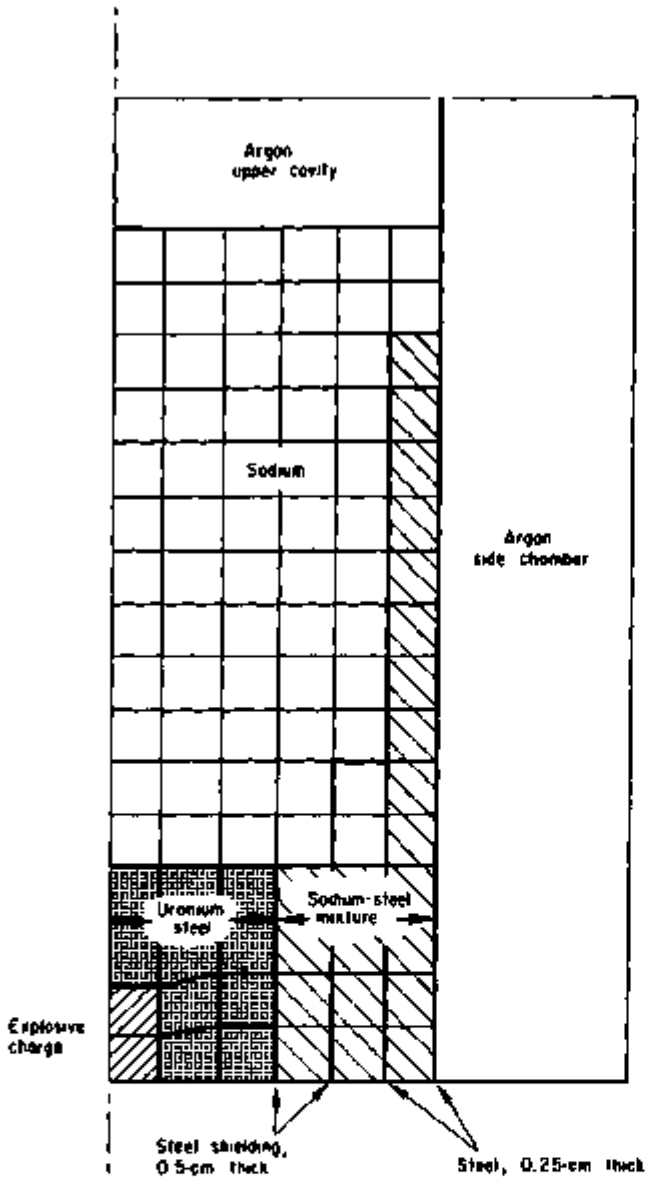

Fig. 17.
Initial Lagrangian Mesh Configuration for the REXCO-H Computation for the Cadarache Experiment. ANL Neg. No. 900-728.

region may be considered to be reasonably accurate. At least the computed pressures in these undistorted surface cells are not contradicted by the experimentally measured pressures.

The major uncertainty in the computation lies in the equations of state for the shielding materials. The blankets are simulated by a mixture of closely packed uranium and steel rods with an average density of 12.7 gm/cm^3. The concentric stainless steel cylindrical reflectors were so closely spaced (1-mm spaces) that it was necessary to include within a single computational grid cell several alternating layers of steel reflectors and liquid sodium. As a consequence, a single cell must be treated as a mixture of materials, and a representative average equation of state for the mixture must be devised. The mixture equation of state was based upon a composite Hugoniot constructed from the individual Hugoniot curves for the constituent materials. The individual

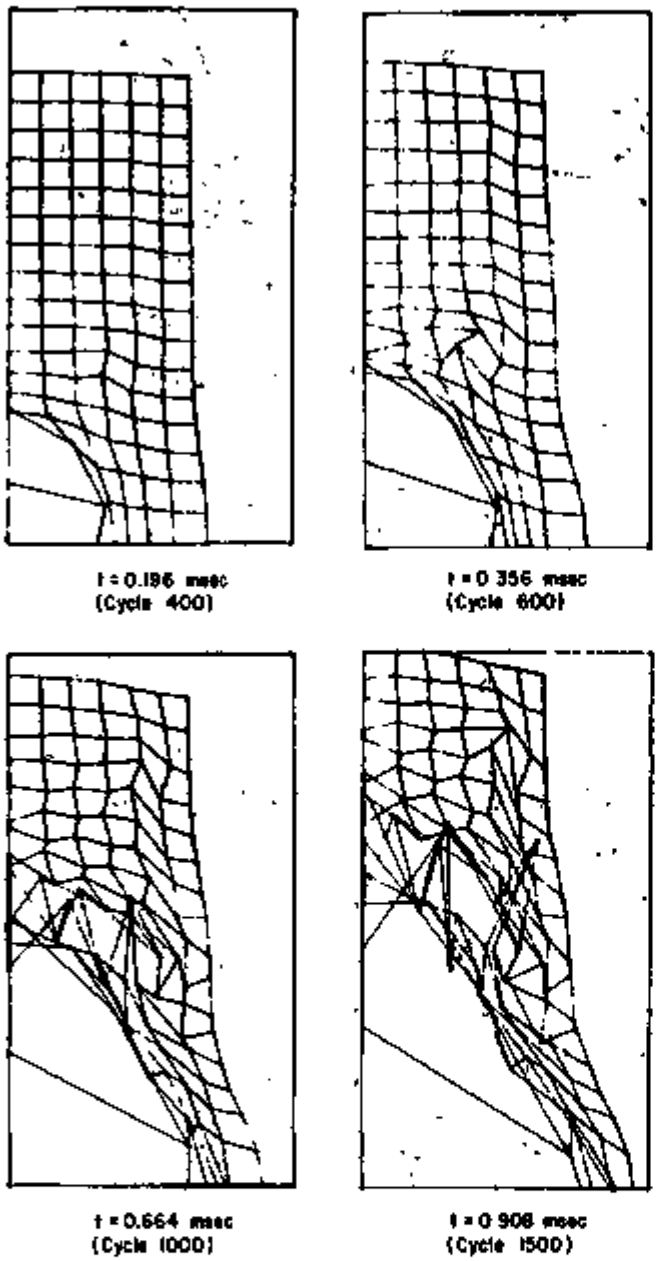

Fig. 18.
Distortion Sequence of the Lagrangian Mesh for the Cadarache Computation.

Hugoniot curves were based upon Ref. 9 and derived from a shock fitting of the form of Eq. 3 with the values of a and b for each material specified. The specific volume ratio is

$$V = v/v_o = 1 - \frac{u_p}{U} = 1 - \frac{u_p}{a + bu_p}, \tag{6}$$

and the pressure is given by

$$p - p_o = \frac{Uu_p}{v_o} = \frac{(a + bu_p)u_p}{v_o}. \tag{7}$$

For each material, with specified a and b, the Hugoniot curve (p,V) is constructed from Eqs. 6 and 7 by assigning a range of values to the parameter u_p. For a mixture consisting of materials A and B, the mixture Hugoniot (p_H,V_M) can be constructed from the mixing rule

$$V_M = \alpha V_A + (1 - \alpha)V_B \qquad (8)$$

where α is the original volume fraction of material A, and V_A and V_B are found from the individual Hugoniot curves at pressure p_H. The mixture internal energy is given by

$$e_M = e_H + \frac{p - p_H}{\Gamma \rho_M}$$

where the Hugoniot internal energy is

$$e_H = \frac{p_H + p_o}{2} \frac{1 - V_M}{\rho_o} ,$$

the average density is

$$\rho_o = \alpha \rho_{A,o} + (1 - \alpha)\rho_{B,o} ,$$

and the average Grüneisen coefficient is

$$\frac{1}{\Gamma} = \frac{\alpha V_A}{V_M} \frac{1}{\Gamma_A} + \left(1 - \frac{\alpha V_A}{V_M}\right)\frac{1}{\Gamma_B} .$$

The equations of state based upon the above simple mixing rules yielded physically reasonable-appearing results. The success of the method may be attributed in large measure to the similarity of the materials A and B. If widely differing materials were mixed, separate experiments should be conducted to determine the composite equation of state.

D. The Naval Ordnance Laboratory Rupture Model Tests

The fourth experiment analyzed for comparison with the REXCO-H code was run in the apparatus shown in Fig. 4 by the U. S. Naval Ordnance Laboratory. The experiment was designed to measure the plug jump, and, in consequence, as a test of the REXCO-H code it is deficient in certain respects. The code computes the conditions developing during the initial time period before the first millisecond. It is during this period that the most interesting events occur, the shock-wave and major compressibility effects are completed, the vessel failure occurs, and the peak pressure which will subsequently drive the model plug has developed. This peak pressure was computed to be 58.5 psig at 0.534 msec, as shown in Fig. 19. For the experiment the pressure measurements were effectively only

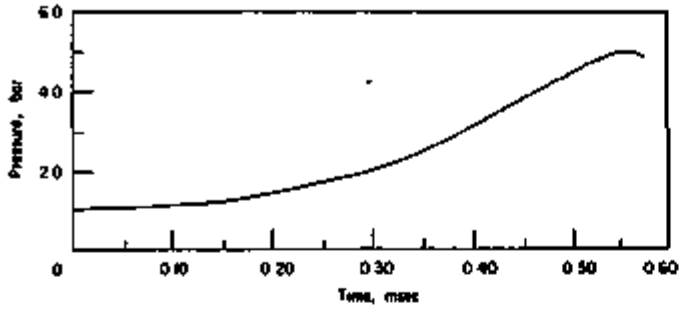

Fig. 19. The REXCO-H Computed Chamber-pressure History for the NOL Rupture Model (126.45-gm PETN/TNT 50/50 Charge). ANL Neg. No. 900-682.

beginning at this time; the reported measured pressures were 49 psig for the sodium temperature of 561°F and 67 psig for 850°F. The average peak pressure for the two experiments is 58 psig. The experimental observations

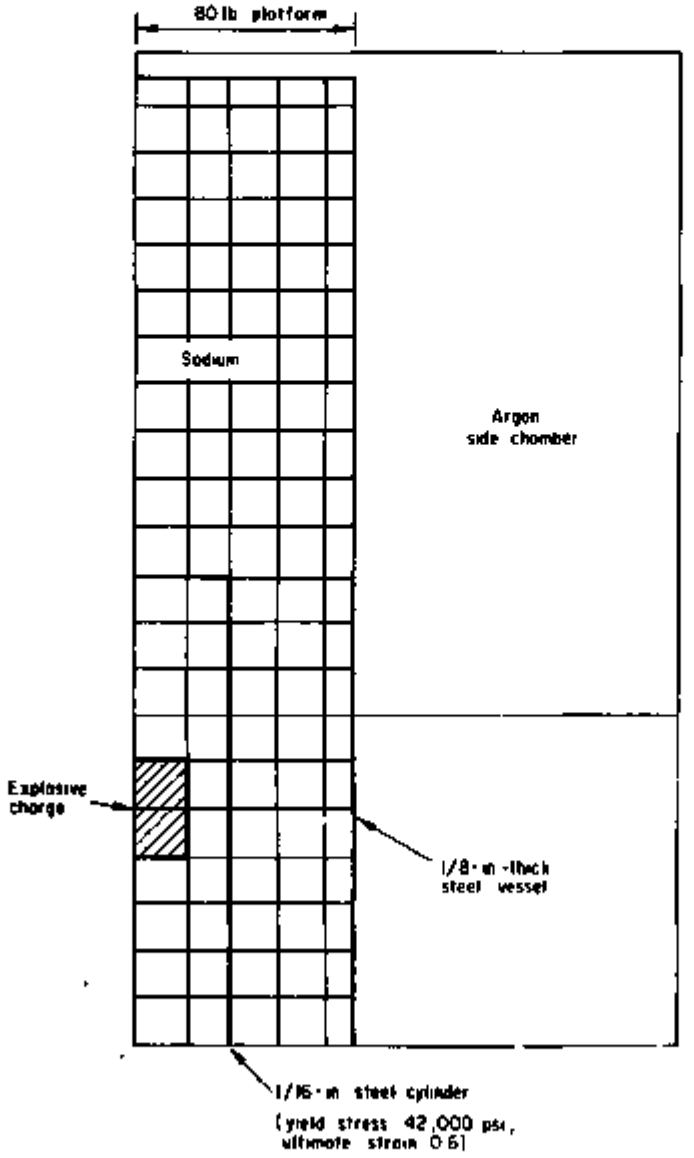

Fig. 20. Initial Lagrangian Mesh Configuration for the NOL Rupture-model Test Comparison. ANL Neg. No. 900-729.

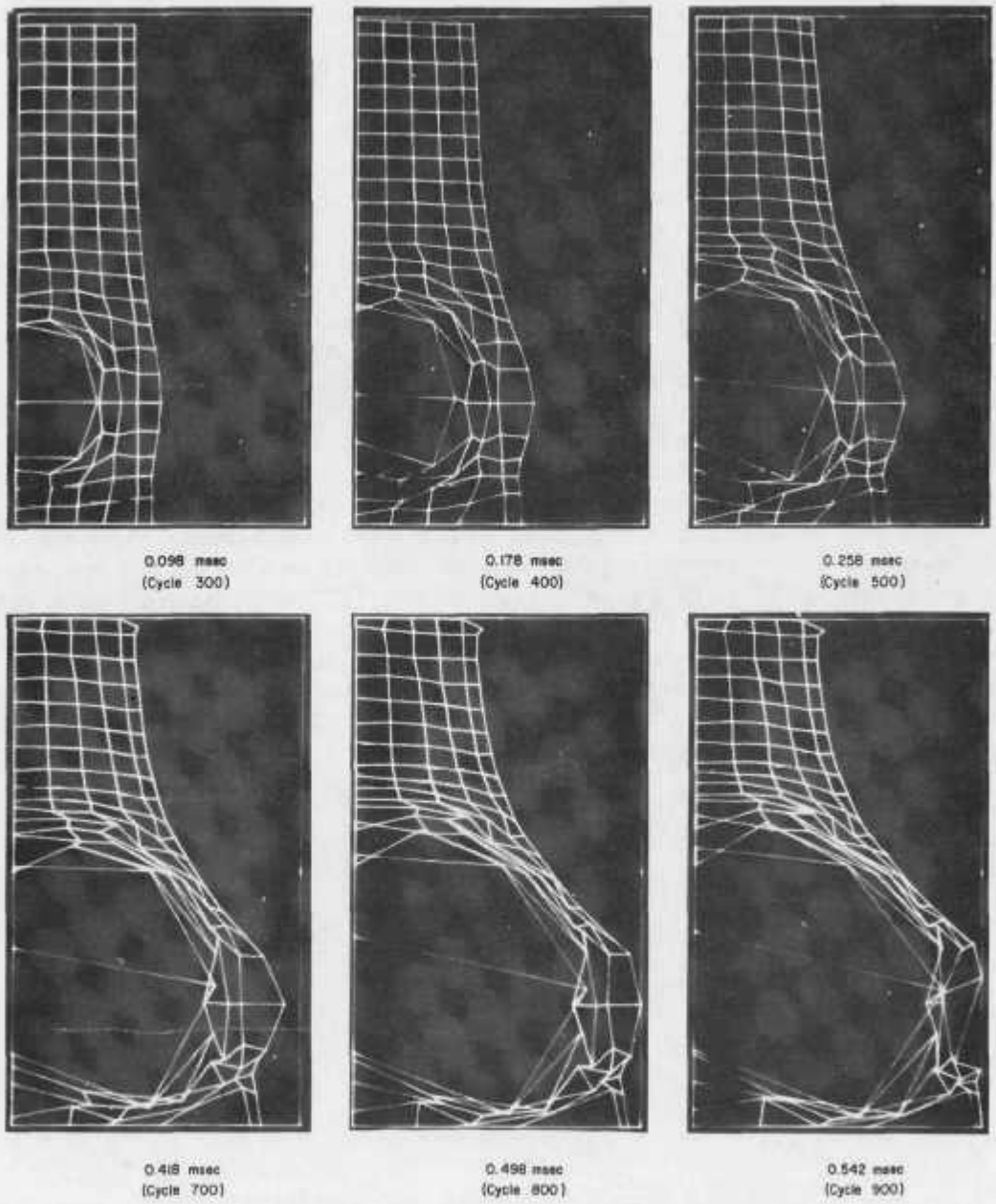

Fig. 21. Distortion Sequence of the Lagrangian Mesh for the Computation of the Explosive Rupture of the NOL Model. ANL Neg. No. 900-674.

were essentially only starting when the peak pressure is reached; at this time the 80-lb plug had scarcely moved. Measurements of the chamber pressure and plug motion extended out to the time when the pressure drops to zero, a duration of the order of 800 msec. The events during this relatively long period are said to be less interesting because the state of the gas driving the plug is well-established in the first millisecond, and the remainder of the time simply involves the well-known ballistics problem of a plug driven by an expanding gas with a given equation of state. The experiment would have been more appropriate if detailed measurements had been made during the first millisecond rather than during the remaining 800 msec. Since no gauges were located within the liquid, shock pressures and times of arrival were not recorded. The only pressure measured was outside of the rupture model; the resulting pressure trace, at the early time, depends upon the vessel-rupture mode, how the sodium ejects from the rupture, the overflow process at the top, and the flashing and mixing processes of the sodium with the surrounding air. The computed sequence of events during the vessel rupture is shown in Figs. 20 and 21. The fact that the measured peak pressure for the hotter sodium was 67 psig compared to 49 psig for the cooler sodium is due to the increased evaporation rate and higher vapor pressure. The shock pressures in the liquid sodium were probably more nearly the same, as indicated by the Cadarache experiments, which found less dependence upon the sodium temperatures. Consequently, the average (of 67 and 49 psig) experimental peak pressure of 58 psig is compared to the REXCO-H computed peak pressure of 58.5 psig. The remarkably good agreement may possibly be more a coincidence, rather than a strong confirmation of the code, in view of the variation from 49 to 67 psig in the experimental measurement. However, it can be concluded that the basic behavior predicted by the REXCO-H code is not contradicted by the experimental observations.

IV. SUMMARY AND CONCLUSIONS

The REXCO-H code is designed as a tool to predict the early response of a nuclear reactor to an accidental excursion. To establish the effectiveness of the code, comparisons must be made with actual physical data. The most appropriate data available are from laboratory experiments in which reactor accidents are simulated by the detonation of small explosive charges in scaled models. Four experiments were selected for comparative studies. The results of the comparisons demonstrated that the REXCO-H code has the capability of predicting accurately the early-time pressure loadings generated in small-model experiments using such chemical explosives as RDX/TNT and PETN/TNT. As a consequence, for full-scale reactor-core explosions of a similar nature, the application of the code can be extended to the analysis of the initial pressure loadings. For the analysis of a hypothetical accident, a representative model of the full-scale explosion must be supplied as input to the code, together with an adequate description of the dynamic behavior of the materials and components involved.

Of the four experiments analyzed, the most decisive for the purposes of the comparison was the bare explosive charge in water. The pressure waves transmitted through the water were measured directly by a battery of piezoelectric gages mounted in the rigid walls of the container. Because of the simplicity of the experiment, possible ambiguities were minimized in the description of the material behavior and processes. The detonation process and the equations of state for the RDX/TNT and the water are reasonably well-known, so that the correlation between the experimental data and the code results can be expected to provide a true measure of the basic code performance. The comparison in Fig. 6 of the code-predicted pressure-time variation at the gauge-3 position with the values measured in the experiment shows a good agreement. The discrepancies in the comparison are minor for explosive work of this nature and are well within the deviations to be expected from the instrumentation system. The frequency response of the system was limited to 20 kHz, so that some cutoff of the sharp pressure peak will occur, and small variations due to lag times are unavoidable. The conclusion to be reached is that the comparison confirms the computation of the early-time pressure waves generated by the explosion. The computed peak pressure at the container roof of 12,035 psi was also confirmed by the measured peak of 12,500 psi in the experiment.

The Cadarache and NOL experiments are perhaps not as well suited for comparison with the code results because the pressure waves transmitted through the liquid were not measured directly. In the NOL experiment a single pressure-time trace were measured in the large chamber surrounding the rupture model (see Fig. 4). The principal objective of the experiment was to study the plug rise, which is a relatively slow process taking place over a time period extending from 50 to over 400 msec. The peak blast pressure in the chamber is reached in 534 μsec, at which time the plug has scarcely moved. The plots shown in the NOL report[4] show only the falling chamber pressure and the plug stroke.

In spite of the apparently good comparison of the computed peak pressure with the average peak pressure for the two experiments, confidence in the comparison could be improved by more appropriate instrumentation in the experiments. The response time of the instrumentation should be designed to give detailed measurements during the more important early events in the first millisecond. The gauge location should be improved by direct contact with the fluid, and more gauges should be used to obtain a pressure distribution. The pressure measured by the gauge located in the side chamber depends to an uncertain extent upon the complex physical processes which take place when the escaping liquid sodium surges through the ruptured vessel wall and mixes with the surrounding chamber air. A further uncertainty involves the effects of the mode of rupture and the strength of the vessel wall upon the initial pressure buildup in the chamber.

The Cadarache experiment is perhaps somewhat better suited for comparative purposes with the code than the NOL experiment. Although the pressures in the liquid were not measured directly, the pressure gauges were mounted in the roof, 5 cm above the liquid surface of the sodium, rather than in the side wall of the surrounding chamber. The early-time pressure in the space above the liquid is much less dependent upon the mode of vessel failure and the mechanics of the escaping sodium jet mixing with the air in the side chamber. The experimental configuration was quite complex, and the computed peak pressure of 18,000 psi agrees well with the 18,230 psi average for two experiments. In view of the uncertainty of the equations of state applied to the mixed materials surrounding the charge, and the gross distortions permitted without rezoning of the computational procedure, the good agreement between the measured and computed peak pressures may be in part fortuitous. Questions may yet be raised concerning the performance of the code for complicated configurations. Clearly, however, the experiment in no way indicates unsatisfactory code performance.

Good agreement was obtained between the REXCO-H computed results and the data from the three experiments mentioned above: the bare charge, and the Cadarache and NOL experiments. The agreement was not good for the confined-charge configuration shown in Fig. 2. In the experiment the peak pressure measured by gauge 3 was 0.24 kb. Without the confining structure, the peak measured pressure was 1.59 kb, so the effect of the structure was to attenuate the peak pressure reaching the tank wall by a factor greater than six. The REXCO-H computed pressure at the gauge-3 position was 0.6 kb, compared to a computed peak for the bare charge of 1.91 kb. Hence, the computed effect of the confining structure is to reduce the peak pressure by a factor of only slightly greater than three. The reason for the discrepancy apparently lies in the uncertainty of the elastic-plastic description of the dynamic behavior of the lead shot. The assumption that the lead shot constitutes a homogeneous isotropic medium for the lower pressures (less than 20 kb) probably leads to considerable error. A second, probably minor, source of error is the effect of the heavy diagrid plate structure supporting the lead shot. This diagrid was not included in the computational model; a strong second shock, reflected from the bottom, reached the wall in the computation. This strong second shock was not evident in the experiment.

The conclusion to be reached on the basis of the comparisons of the code results with the experiments described above is that the REXCO-H code computations are consistent with the pressure measurements for the early times following an explosion. For the most simple configuration, the bare charge in water, the experimental measurements were detailed and excellent agreement with the computed results was obtained. The question can be raised concerning the performance of the code for more complex configurations. The experiments do not really answer this question adequately, although the Cadarache configuration was quite complex and good agreement was obtained for the initial times up to about 1 msec. Beyond this time the grid distortion, excessive already much earlier in the interior regions, progresses to the neighborhood of the containment roof, so that the computed pressures in that area are no longer reliable. The obvious recommendation to improve the performance of the code is to develop methods to extend the time range over which reliable computations can be made. Rezoning provides a partial remedy, but by itself is not sufficient to extend the computations significantly into the millisecond range for the high-explosive model tests. For the lower pressures at the later times the elastic-plastic descriptions should be improved, together with the thermodynamic equations of state of both individual and composite materials.

From the examination of available experiments, it is apparent that a special experimental program should be designed with the specific objective of testing the code performance. Specific tests should be planned to reveal intermediate and internal features of the physical processes involved, and to provide more detailed and accurate equations of state, especially for multicomponent material mixtures.

Verification of the code for the highly transient phenomena simulated by existing high-explosive tests does not necessarily imply that the application of the code can be extended, without modification, to the slower excursion phenomena of a prototype reactor accident. Particular attention should be given to heat-transfer effects. Experiments designed for controlled excursion simulation should be run to test the rate dependence of the REXCO-H code.

However, in terms of structural damage, the most important destructive mechanisms occur during the very early period of sharp peak pressures, and this period is well described by the REXCO-H code.

APPENDIX A

The Mathematical Model

1. The Hydrodynamic Equations

The REXCO-H code is designed to compute the hydrodynamic response of a primary reactor-containment system undergoing a high-energy excursion. The response is termed "hydrodynamic" for the range of conditions prevailing during an energy release so high that the shear-stress actions are negligible compared to the dominating hydrodynamic pressure gradients. In general, the material shear strength is no greater than a few kilobars, so for shock pressures in the neighborhood of 100 kb the material can with accuracy be treated as a fluid; good results can be expected for pressures down to 50 kb. For metals below 50 kb, measured wave velocities exceed the values computed on a purely hydrodynamic basis. Since the elastic ranges up to the order of 10 kb, an elastic precursor may develop during a pressure buildup and persist ahead of the shock for shock strengths as high as several hundred kilobars. However, in terms of damage, these precursors can be ignored in comparison to the effects of the shock wave. For the hydrodynamic range of conditions the mechanics of the affected regions can be described by the system of continuum field equations for the conservation of mass, momentum, and energy, together with an equation of state:

$$\text{mass:} \quad \frac{D\rho}{Dt} + \rho \ \text{div} \ \bar{u} = 0; \tag{A1}$$

$$\text{momentum:} \quad \rho \frac{D\bar{u}}{Dt} = - \ \text{grad} \ p; \tag{A2}$$

$$\text{energy:} \quad \frac{De}{Dt} + p \frac{Dv}{Dt} = 0; \tag{A3}$$

$$\text{state:} \quad p = f(v,e); \ v = 1/\rho. \tag{A4}$$

There are four unknown functions of position and time. The thermodynamic state is described by the fields of pressure p, density ρ, and internal energy e; the state of motion is described by the velocity vector field $\bar{u}$.

The mathematical model for a given reactor configuration includes the above system of equations together with prescribed initial conditions. The model is simplified by considering only those cases possessing axial symmetry. A cylindrical coordinate system is introduced to describe the radial (r) and axial (z) locations. The radial and axial components of the velocity vector are u and w. The differential operators are then

$$\left.\begin{aligned} \frac{D}{Dt} &= \frac{\partial}{\partial t} + u\frac{\partial}{\partial r} + w\frac{\partial}{\partial z}\ ; \\ \text{grad} &= \left(\frac{\partial}{\partial r}, \frac{\partial}{\partial z}\right)\ ; \\ \text{div}\ \bar{u} &= \frac{\partial u}{\partial r} + \frac{\partial w}{\partial z} + \frac{u}{r}\ . \end{aligned}\right\} \qquad \text{(A5)}$$

The solution to a problem in this system is the set of functions $\bar{u}(r,z,t)$, $\rho(r,z,t)$, $e(r,z,t)$, and $p(r,z,t)$ which satisfy the mathematical model.

The field equations as formulated above with the position (r,z) taken to be an independent variable is referred to as the "Eulerian description." Difficulties are encountered in the use of this description when the changing locations of interfaces between materials must be known at all times. As deformations occur in the reactor configuration, it is necessary during the computation to follow the motions of the interfaces in order to apply the proper equation of state and material properties to each region. The most natural way to follow the motions of the points of the medium is to write explicitly the coordinates (r,z) of each material point. The material point itself must be identified by some label (R,Z) called the "Lagrangian coordinates" of the material point. This label vector can be chosen as the initial position vector (r,z) of the material point. There is assumed to exist a one-to-one transformation continuous in time between the material points and their locations:

$$r = r(R,Z,t);\quad z = z(R,Z,t). \qquad \text{(A6)}$$

The radial velocity component of the material point (R,Z) is then

$$\dot{r}(R,Z,t) = \partial r(R,Z,t)/\partial t. \qquad \text{(A7)}$$

We can regard the problem now in either of two (vector) spaces: the Lagrangian coordinate space of material particles which maintains an invariant configuration with time, or the Eulerian coordinate space which describes the actual changing positions of the deforming medium. From the point of view of the Lagrangian space, we look at the material point (R,Z), at an interface, say, as the independent variable and ask about its position (r,z). Conversely, for the field Eqs. A1-A3, we look first at the spatial location (r,z), and from the inverse of Eq. A6 we discover which material point (R,Z) is at that position at time t. The radial field velocity, for example, at this position is then

$$u(r,z,t) = \dot{r}(R,Z,t). \qquad \text{(A8)}$$

Similarly, the radial field acceleration at position (r,z) is related to the radial acceleration of the material point (R,Z) by

$$\frac{Du}{Dt}\,(r,z,t) = \ddot{r}(R,Z,t)\ . \qquad (A9)$$

The volume Ψ_o of the point set $\{(R,Z)\}$ of a given region of the original material configuration is related to its deformed volume $\Psi(t)$ (of the set of corresponding points $\{(r,z)\}$) by the familiar integral transformation

$$\int_{\Psi_o} J\ d\Psi_o \rightarrow \int_{\Psi(t)} d\Psi\ ,$$

where J is the Jacobian or functional determinant of the transformation (where r and z are functions of R, Z, t):

$$J = \frac{r}{R}\left(\frac{\partial r}{\partial R}\frac{\partial z}{\partial Z} - \frac{\partial r}{\partial Z}\frac{\partial z}{\partial R}\right).$$

Since the volumes Ψ_o and Ψ contain the same material in the original and deformed states, respectively, the conservation of mass requires

$$\int_{\Psi_o} \rho_o(R,Z,T)\ d\Psi_o = \int_{\Psi(t)} \rho(r,z,t)\ d\Psi\ .$$

Because of the above volume-integral transformation,

$$\int_{\Psi(t)} \rho d\Psi = \int_{\Psi_o} \rho J d\Psi_o\ .$$

It then follows directly that

$$\int_{\Psi_o} (\rho_o - \rho J)\ d\Psi_o = 0\ .$$

Since the integrand is arbitrary, it necessarily must be identically zero. Hence, the mass conservation is expressed as a differential equation, where r and z are functions of R, Z, and t:

$$\text{mass:}\quad \rho_o(R,Z,t) = \rho(r,z,t)\ J\ . \qquad (A1')$$

The momentum and energy equations in the Lagrangian space (where r, z, and p are functions of R, Z, and t) become

$$\text{momentum:} \quad \begin{cases} \ddot{r}(R,Z,t) = -\dfrac{1}{\rho_o}\dfrac{r}{R}\left(\dfrac{\partial p}{\partial R}\dfrac{\partial z}{\partial Z} - \dfrac{\partial p}{\partial Z}\dfrac{\partial z}{\partial R}\right); \\ \ddot{z}(R,Z,t) = \dfrac{1}{\rho}\dfrac{r}{R}\left(\dfrac{\partial p}{\partial R}\dfrac{\partial r}{\partial Z} - \dfrac{\partial p}{\partial Z}\dfrac{\partial r}{\partial R}\right); \end{cases} \tag{A2'}$$

$$\text{energy:} \quad \dot{e}(R,Z,t) = -p\,\dot{v}(R,Z,t). \tag{A3'}$$

2. The Finite-difference Equations and Cell Distortion

A variety of numerical procedures have been used to derive approximate solutions to the mathematical model described above. The general computational procedure for the Lagrangian formulation can proceed somewhat as follows. At the initial time a grid as shown in Fig. A1 is laid out covering the reactor configuration.

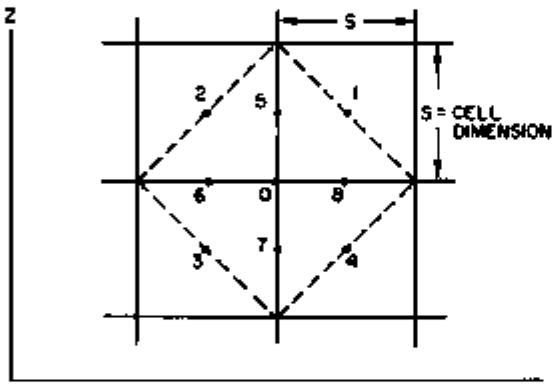

Fig. A1.
An Initial Finite-differencing Grid Configuration.

The grid embedded in the material will deform in the Eulerian (r,z) space but will remain invariant in the Lagrangian (R,Z) space. The deformation is computed for finite time steps based upon the acceleration of the points. For example, the radial velocity for point 0 is

$$\dot{r}_{t+\Delta t/2} = \dot{r}_{t-\Delta t/2} + \ddot{r}_t \Delta t,$$

and the displacement is

$$r(R_o,Z_o,t+\Delta t) = r(R_o,Z_o,t) + \dot{r}_{t+\Delta t/2}\Delta t.$$

These are linear approximations, and the error of order $O(\Delta t^2)$ can be controlled by the choice of Δt.

From the computed displacements, the volumes of the deformed cells are determined, and the new densities are derived from the conservation of mass. The pressure and internal energy of the cell are then determined from the simultaneous Eqs. A3' and A4:

$$e_{t+\Delta t} = e_t - \frac{1}{2}\left(p_{t+\Delta t} + p_t\right)\left(v_{t+\Delta t} - v_t\right) ;$$

$$p_{t+\Delta t} = f\left(v_{t+\Delta t},\ e_{t+\Delta t}\right) .$$

The method outlined above describes the procedure for accomplishing the numerical integration with respect to t. The most serious question concerning this integration is that of convergence. An artificial viscosity is introduced to dampen oscillations in regions of high gradients, and a stability parameter limits the maximum Δt to keep the forward-time-differenced disturbance within the region of influence.

The entire computation, then, is seen to hinge upon the computation of the material-point trajectories based upon the computation of their accelerations. The accelerations are determined from the pressure forces, and it is here where the major computational difficulty occurs. The pressure force may be computed in the Lagrangian space for the right-hand side of Eq. A2', or the force may be computed directly from the pressure gradient in the actual (Eulerian) space expressed by the right-hand side of Eq. A2. The first alternative is more simple because the grid is fixed in the Lagrangian space. The derivatives, for the pressure, for example, are derived from the Taylor's series expansion:

$$p_8 - p_o = \frac{S}{2}\left(\frac{\partial p}{\partial R}\right)_o + \left(\frac{S}{2}\right)^2\left(\frac{\partial^2 p}{\partial R^2}\right)_o + O(S^3);$$

$$p_6 - p_o = -\frac{S}{2}\left(\frac{\partial p}{\partial R}\right)_o + \left(\frac{S}{2}\right)^2\left(\frac{\partial^2 p}{\partial R^2}\right)_o + O(S^3).$$

Combination of these two expressions gives

$$p_8 - p_6 = S\left(\frac{\partial p}{\partial R}\right)_o + O(S^3).$$

By neglecting terms of third order,

$$\ddot{r}_o = -\frac{1}{\rho_o}\frac{r_o}{R_o}\frac{1}{S^2}\left[(p_8 - p_6)(z_5 - z_7) - (p_5 - p_7)(z_8 - z_6)\right].$$

The accuracy is of second order in the grid spacing S and apparently independent of cell distortion, provided, of course, that no side of the cell collapses to zero (or turns "inside out" destroying the contiguous ordering of the material points).

It can be argued, however, that this accuracy is illusory when the actual distortion is viewed in the Eulerian space shown in Fig. A2.

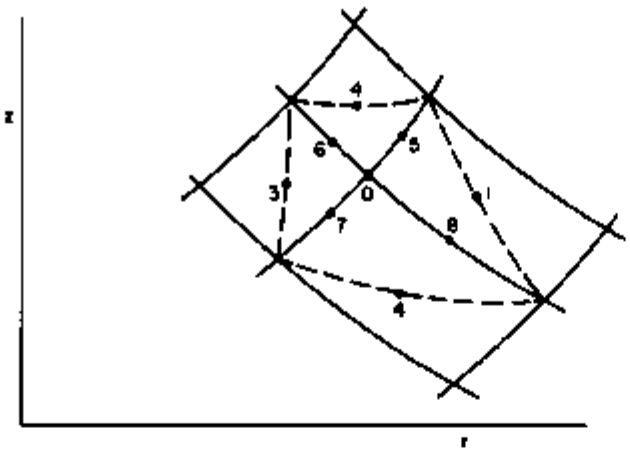

Fig. A2.
The Distorted Grid Configuration in the Eulerian Frame

The above combination of $p_8 - p_o$ and $p_6 - p_o$ should be thought of as taking the average of the two pressure gradients:

$$\frac{p_8 - p_6}{L} = \frac{1}{2}\left[\frac{p_8 - p_o}{L/2} + \frac{p_o - p_6}{L/2}\right],$$

where L is the distance between Points 8 and 6. It is clear that the contribution of $p_o - p_6$ should be greater than that of $p_8 - p_o$ to the approximation of the pressure gradient at Point 0, simply because Point 8 is more remotely located than Point 6. Hence, a weighting factor should be derived, with the result that the second-order terms in the Taylor's series will not cancel. To carry along the second-order terms, it becomes necessary to solve simultaneous equations for both the first and the second derivatives, which considerably complicates the numerical procedure. If the second-order terms are neglected, then the accuracy will deteriorate as the cells distort, even when the computation is done in the distortionless Lagrangian space.

For this reason, the pressure gradient in REXCO-H* is computed directly in the Eulerian space, where the weighting is automatically taken care of in the Taylor's series expansion which involves the actual displacements between material points. The effect of the cell distortion upon the accuracy appears more directly than when the gradient is computed in the Lagrangian space. An index of the maximum cell distortion is monitored for each time cycle (i.e., a complete spatial computation at a fixed time step). The index compares the lengths of opposite sides of the cell (and also diagonals), so that if one side collapses to zero the index will become infinite. In general, when the index exceeds a preset value the computation will stop and the problem is reinitialized with a new rectangular grid. The relative effects of this rezoning procedure and comparison with experiments are discussed in Sect. III.

*See Ref. 1 for details.

3. Rezoning

A rezoning option is included with the REXCO-H code to reduce the type of error resulting from cell distortion. The finite-differencing grid can be rezoned after any number of cycles. The decision to rezone can be made on the basis of visual examination of the distorted grid (e.g., see Fig. 7) or based upon a numerical measure of the cell distortion. A distortion index can be defined for each cell in terms of the dimensions shown in Fig. A3, and the value for the most distorted cell can be monitored at each computational cycle.

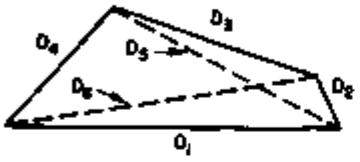

Fig. A3.
Distances Used to Define the Distortion Index

The optimum policy to minimize errors due to cell distortion alone is to rezone after each computational cycle. However, other errors are introduced by the rezoning process. So a game is involved in which errors of one type must be traded off against other errors, with the object of achieving maximum overall accuracy. Unfortunately, the rules of this game are not yet known, and the procedure for deciding when to rezone must be based both upon experience gained by comparing alternative computational procedures, and by the laborious method of examining key variables at each cycle to see that numerical values are physically reasonable and consistent with the conservation laws. Supplementary checks must also be made by comparison with known experimental data.

The finite-differencing grid used in the REXCO-H code is fixed to the material particles (i.e., a Lagrangian grid). Rezoning, in the sense used here, means simply that the grid is changed with respect to the particle. As a consequence, even for a grid fixed in space (an Eulerian grid) when particles flow in or out of a grid cell, the grid is actually changing with respect to the particles and rezoning is effectively taking place. For example, a code such as the PIC code, which retains a fixed grid, is in effect undergoing a rezoning at each computational cycle; while distortion errors are eliminated, rezoning errors are accumulating. The rezoning errors arise because a cell variable, such as the fluid density, can have only one representative value for the set of particles in the cell. Some sort of average must be taken over the constituent particles of a cell. Each time the particles in a cell change, an additional error due to this averaging process occurs.

As an example, consider a rezoning (i.e., a transfer of particles between cells) in which the average density in a cell is given the obvious value of the sum of the constituent particle masses divided by the cell volume:

$$\rho = \frac{\Sigma \rho_i V_i}{V} \quad .$$

Then ρV represents the actual total mass in the cell, and the conservation of mass is satisfied. Similarly, if the average velocity is defined as the sum of the momenta of all particles in the cell divided by the mass,

$$\bar{u} = \frac{\Sigma \rho_i u_i V_i}{\rho V} ,$$

then $\rho \bar{u} V$ represents the total momentum in the cell, and the conservation of momentum is satisfied. Unfortunately, the kinetic energy $\rho V \bar{u}^2/2$ is not the total kinetic energy in the cell. To conserve the kinetic energy in the cell a different average velocity must be used:

$$\bar{u}^2_{KE} = \frac{1}{\rho V} \Sigma \rho_i \bar{u}_i^2 V_i .$$

Whatever average velocity is used there will be an error in either the kinetic energy or the momentum conservation. It is possible to conserve the total energy of the cell by defining an average internal energy e to satisfy

$$V\left(e + \frac{\bar{u}^2}{2}\right) = \Sigma \rho_i \left(e_i + \frac{\bar{u}_i^2}{2}\right) V_i .$$

Since ρ and e are now specified for the cell, an "average" cell pressure can be defined by the equation of state

$$p = f(\rho, e) .$$

The forces produced by these pressures may be quite different from the forces produced by the constituent-particle pressures. The effect, then, of imposing an internal energy to satisfy the conservation of energy for the rezoning is to introduce a spurious set of forces that will dynamically distort the system. Unless these extraneous forces are damped out, each rezoning will cause the computation to deviate further from a true solution. The growth or decay of disturbances is dependent upon the stability of the computational procedures and is discussed next.

4. Stability and Artificial Viscosity

For flows involving shock waves, numerical instabilities can arise, resulting in highly fluctuating numerical values. The introduction of a von Neumann-Richtmyer type of artificial viscosity can tend to dampen these numerical fluctuations by spreading out the pressure discontinuity over several mesh spaces. The artificial viscosity q is added to the pressure p in each cell, and the sum replaces the actual pressure in the momentum and energy equations (but not in the equation of state). An example of how the artificial viscosity tends to "smear out" the

discontinuity is shown in Fig. A4. The explosive is contained in two located cells at the center of a large cylindrical tank containing water.

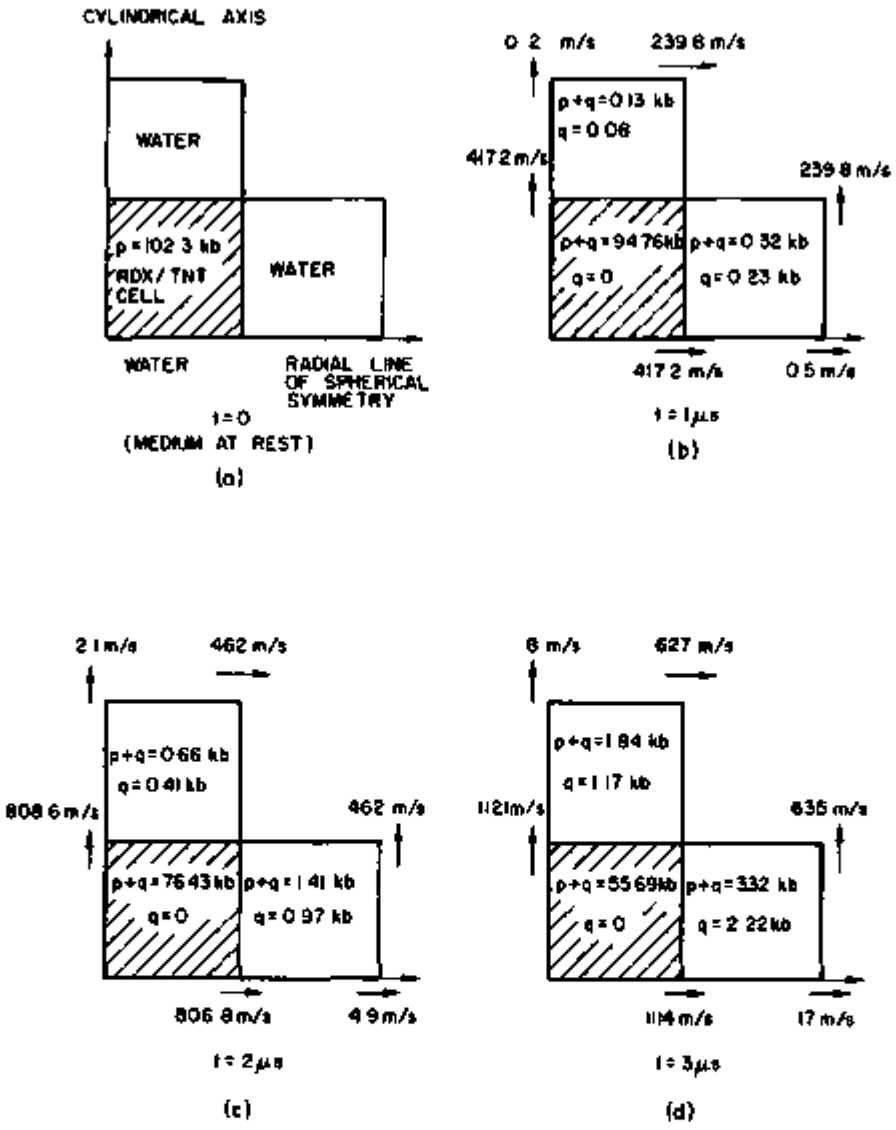

Fig. A4. Illustration of the Spreading Effect of the q Pressure

The effect upon one of the cells in the upper quadrant of the radial plane is shown in Fig. A4. The detonation process is assumed to be complete at time t = 0, the explosive is at a high pressure of 102.3 kb, and no motion has yet ensued. At the end of 1 μsec, the explosive charge has begun to expand, and the motion of the outer force has compressed the surrounding water. The artificial viscosity term is computed for compressed cells by the equation

$$q = (1.2)^2 \rho_o A \frac{1}{\rho^2} \left(\frac{\Delta\rho}{\Delta t}\right)^2 \qquad \text{(A10)}$$

For an expanding cell, q is set equal to zero. At the end of 3 μs the outer faces of the RDX/TNT cells have accelerated to velocities in excess of 1100 m/sec, compressing the surrounding water cells. Due to the compression alone the pressure in the water cell (on the radius) is p = 1.1 kb; however, the "viscous" pressure due to the rate of compression is q = 2.22 kb, producing a total resisting stress of 3.32 kb, or increasing the resisting pressure p by a factor of three. This increased effective pressure in turn will transmit an accelerating force to the next adjacent water cell, and in this way will have both a damping influence upon the growth of the expansion rate of the RDX/TNT cell, and also tend to "smear out" the motion to cells downstream of the actual shock wave.

An example of the difficulty that can be introduced by the artificial viscosity is shown in Fig. A5. The value of q in the cell shown on the

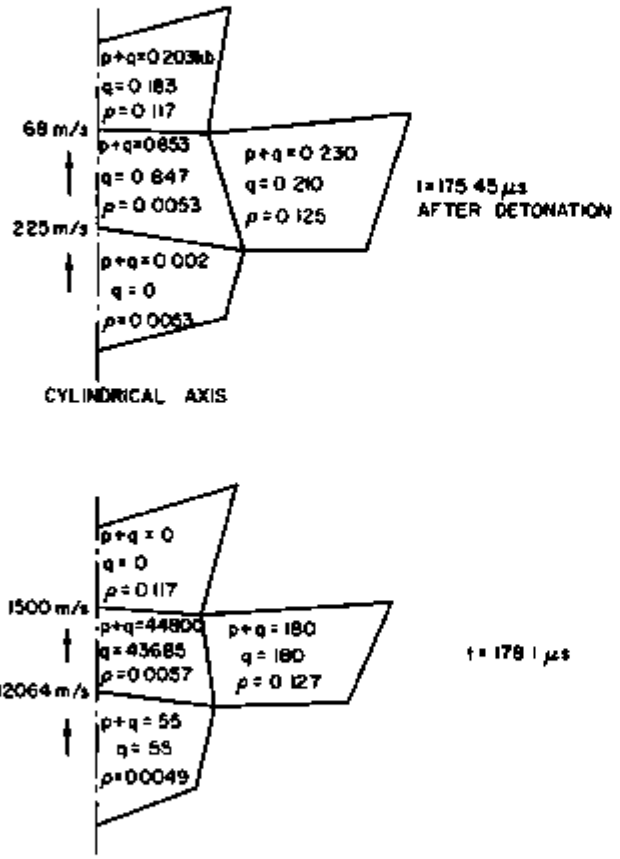

Fig. A5.
Example of Viscous Pressure "Blowing up" for Cell on Axis.

axis at 175.45 μsec after detonation is 0.847 kb. Just 2.65 μsec later the value of q has shot up to the physically impossible high value of 43,685 kb. The overall energy conservation was violated and the computation stopped. The velocities have also increased to impossibly high values due to the high pressure gradients created in the very low density ($\rho \doteq 0.005$ gm/cm^3) fluid. The high velocities in turn set up higher q values, with the net result that the artificial viscosity is a source of instability rather than a dampening influence. In the case shown in Fig. A5 the cause of the great increase in q is not due directly to cell distortion, but to the small ρ and the small Δt. (The value of

Δt is determined from the White stability condition.) These effects are amplified because ρ and $\Delta\rho/\Delta t$ appear as quadratic terms.

An improvement may be achieved by using a linear form.* The phenomenon illustrated here is probably similar to the so-called "bubbling of particles" at the axis as referred to by Amsden.[10] His remedy was to set q equal to zero on the axis (and also at rigid walls). For the case illustrated in Fig. A5 this was done, and the computation advanced satisfactorily without the abnormal increase in q.

When q was set equal to zero at the start of the program, however, the undesirable asymmetry was exaggerated. For this reason q was not set equal to zero on the axis until the undesirable effects were detected by monitoring the total energy conservation. When this criterion was violated, the program was stopped and restarted (50 computational cycles back in time) with q set equal to zero on the axis.

It was found that q can be set equal to zero everywhere in the later stages of the computation without incurring instabilities and with results not significantly different from those with the inclusion of q. The reason for this is that the finite-difference equations contain hidden diffusive effects not present in the original differential equation. These diffusive effects are the result of neglecting the higher-order terms in the transformation:

differential equations $\longrightarrow$ finite-difference approximate form + neglected higher-order terms .

The hidden diffusive terms arising from the approximate nature of the (linear) finite-difference form can be derived explicitly by making the inverse transformation:

finite-difference approximate form $\longrightarrow$ differential equations (original nondiffusive) + diffusive terms (arising from neglected terms)

The transformations in either direction are accomplished by Taylor series expansions.

Thus, we see that the finite-difference approximate form does not exactly represent a nondiffusive differential equation, but actually contains diffusive effects which tend to smear out discontinuities just as physical (or artificial) viscous terms in some exactly equivalent differential equation. Such small discontinuous numerical disturbances arise at each computational cycle because of the finite-difference character of the equations. It is for this reason that originally stable differential equations may have unstable finite-difference representations. The additional diffusive terms may not always have a

---

* See, e.g., G. Maenchen and S. Sack, "The Tensor Code" in *Methods in Computational Physics*, Vol. 3, Academic Press (1964) also discussion in Appendix B.

stabilizing influence. Examination of the algebraic signs may reveal "negative damping" effects. Artificial viscosity terms can then be devised to compensate for these spurious diffusive terms.

Numerical instabilities may be due purely to the computational procedure and may have no meaningful physical interpretation. For example, in Fig. A5, the apparently unstable growth of the viscous pressure has been referred to as a "bubbling phenomenon" taking place at the axis. A closer examination showed that the trouble is in the simultaneous solution of Eq. A10 and the semi-empirical equation for the White stability parameter W:

$$W = \frac{c^2(\Delta t)^2}{A} + 4a\left|\frac{\Delta v}{v}\right| ,$$

where v is the specific volume, the constant 'a' is chosen to be 1.2, and c is the local sound speed. The stability criterion requires

$$0.035 < \left(\frac{W}{1.2}\right)^2 < 0.14 . \qquad \text{(A11)}$$

The purpose of the criterion is to limit the length of the time step Δt so that a small numerical disturbance can extend no further than the local cell spacing (the Courant condition). The lower limit is chosen to avoid excessive computations resulting from Δt being unnecessarily small. The disturbance is assumed to propagate with the local sound speed c:

$$c^2 = -v^2 \, (\partial P/\partial v)_s .$$

The value of $P = p + q$ is used,* rather than p alone, to be consistent with the assumption that P provides the driving force for the fluid motions (i.e., P now replaces p in the momentum and energy equations). Isentropic (constant s) equations of state can be assumed of the forms

$$\begin{cases} \text{gas:} & pv^\gamma = \text{constant} \\ \text{condensed material:} & p = p_B[(v_o/v)^\gamma - 1] . \end{cases}$$

For q given by Eq. A10, the sonic speed is

$$\begin{cases} \text{gas:} & c^2 = v(\gamma p + 2q) \\ \text{condensed material:} & c^2 = v[\gamma(p + p_B) + 2q] . \end{cases}$$

---

* See R. Frank and R. Lazarus, "Mixed Eulerian-Lagrangian Method" in *Methods in Computational Physics*, Academic Press (1964), p. 62, where c^2 is assumed to be γPv. With equal physical logic it could be argued that the viscosity q ought be zero for an assumed isentropic disturbance.

The White stability number is then given by

$$\text{gas:}\quad \left(\frac{W}{1.2}\right)^2 = v\,\frac{(\gamma p + 2q)}{A}\left(\frac{\Delta t}{1.2}\right)^2 + 4\left|\frac{\Delta v}{v}\right| \qquad \text{(A12)}$$

$$\text{condensed material:}\quad \left(\frac{W}{1.2}\right)^2 = \frac{v[\gamma(p + p_B) + 2q]}{A}\left(\frac{\Delta t}{1.2}\right)^2 + 4\left|\frac{\Delta v}{v}\right| .$$

The coupling between q and Δt through Eqs. A10, A11, and A12 is now evident. If q should increase abruptly, then Δt will be cut down by the limits set by Eq. A11. As a consequence, for the next computational cycle the value of q computed from Eq. A10 will be further increased. The resulting rapid growth of q is apparently the cause of the instability shown in Fig. A5. Once the cause is recognized, it is easy to devise corrective steps. In this particular case the coupling between Eqs. A10 and A12 can be eliminated simply by removing q from Eq. A12. This can be rationalized by regarding the sonic speed as a thermodynamic state property characteristic of disturbances so small that q is negligible (consistent with the assumption that c is the speed of a small isentropic disturbance):

$$c^2 = v^2(\partial p/\partial v)_s .$$

The point to be emphasized in the above example is that numerical stability considerations, in general, hinge upon arithmetical rather than heuristic physical arguments. For example, the artificial viscosity is introduced to stabilize computations. Although it may be given a physical interpretation, the optimal form is based upon computational effectiveness rather than a physical model. The use of the artificial viscosity in REXCO-H and comparisons with some other forms are discussed further in Appendix C.

5. The Elastic-Plastic Equations

The second test case considered for comparison with the REXCO-H code is that of a small charge enclosed within a breeder section simulated by lead shot, as shown in Fig. 2. The hydrodynamic equations alone were found to be insufficient to account for the attenuation of the initial pressure wave achieved in the experiment. The correlation of code results with the experimental data was improved by introduction of the equations for plastic flow. The equations are those presented by Wilkins,[5] and the details of the code are given by Cinelli, Gvildys, and Fistedis.[6] The lead shot is considered to be a perfectly plastic material obeying the von Mises yield condition.

The assumptions make by Wilkins are summarized below.

The plastic-flow condition is based upon a yield condition between the stress deviators:

$$f(s_i) = 0; \; i = 1, 2, 3. \tag{A13}$$

The principal stress deviators are

$$s_i = \sigma_i + p \tag{A14}$$

where σ_i are the principal stresses normal to mutually orthogonal planes of zero shear and p is the hydrostatic pressure:

$$p = -\frac{1}{3}\Sigma\sigma_i \; . \tag{A15}$$

The deviators have the property that

$$\Sigma s_i = 0 \; , \tag{A16}$$

so the hydrostatic pressure is independent of the deviator stresses, which may be called the "distortion components" of the stresses. The assumption of perfect plasticity means that the yield condition is time-independent, so that plastic flow occurs at a constant yield stress with no strain hardening. The yield condition is also assumed to be independent of whether the deviator stress is tension or compression.

The principal natural strains are assumed to be composed of elastic and plastic parts:

$$\epsilon_i = \epsilon_{i,E} + \epsilon_{i,P} \; . \tag{A17}$$

The rate of plastic flow along the particle path is assumed to be instantaneously proportional to the stress deviator:

$$\dot{\epsilon}_{i,P} = \dot{\lambda} s_i \; . \tag{A18}$$

Since the sum of the stress deviators is zero, it follows that

$$\Sigma \dot{\epsilon}_{i,P} = 0 \; . \tag{A19}$$

Strain-rate deviators are defined as

$$\dot{\theta}_i = \dot{\epsilon}_i - \dot{\theta} \; , \tag{A20}$$

where the mean normal strain rate is

$$\dot{\theta} = \frac{1}{3}\Sigma\dot{\varepsilon}_i \ . \tag{A21}$$

It follows that a strain-rate deviator has the property that

$$\Sigma\dot{\theta}_i = 0 \ ,$$

so that the plastic strain rates are strain-deviator rates. Also, the continuity condition says that the sum of the principal strain rates is the unit change of material volume:

$$\Sigma\dot{\varepsilon}_i = \dot{V}/V \ , \tag{A22}$$

so that the mean normal strain rate is a measure of the compression of the material:

$$\dot{\theta} = \frac{1}{3}\frac{\dot{V}}{V} \tag{A23}$$

and the strain rate deviators are incompressible flows; in particular, the plastic flow is an incompressible flow. Hence, whereas the elastic portions of the strain are recoverable, the plastic portions are not. As a result, inclusion of the plastic properties in the computation of a pressure-containment material may be expected to exhibit an increased attenuation capability.

The yield condition is a surface in the principal-stress space:

$$f(\sigma_i) = 0. \tag{A24}$$

The plastic-flow rule proposed by von Mises is that the plastic-strain-rate vector be normal to this yield surface. As a result of this assumption, the work done on the material during a loading and unloading cycle is positive for plastic changes, i.e., energy is absorbed by the plastic deformations. A yield surface that satisfies the von Mises condition is the cylinder of radius $\sqrt{2/3}\ Y^0$:

$$(\sigma_1 - \sigma_2)^2 + (\sigma_2 - \sigma_3)^2 + (\sigma_3 - \sigma_1)^2 = 2(Y^0)^2 \ , \tag{A25}$$

where Y^0 is the yield strength in simple tension. In terms of the stress deviators, the yield condition is

$$(s_1 - s_2)^2 + (s_2 - s_3)^2 + (s_3 - s_1)^2 = 2(Y^0)^2 \ . \tag{A26}$$

The computation proceeds as follows. The stress distribution at the beginning of the computational cycle produces particle accelerations. From the ensuing motions the strains are computed. From the resulting strains a new set of stresses are computed, and the computational cycle is repeated for the next time step. The stresses are computed in two steps. First, an elastic stress is computed from Hooke's law:

$$\dot{\sigma}_i = \lambda\frac{\dot{V}}{V} + 2\mu\dot{\epsilon}_i \ , \tag{A27}$$

where λ and μ are the Lamé constants. The hydrostatic pressure is computed from Eq. A15 and the stress deviators from Eq. A14. The intersection of the plane of Eq. A16 passing through the origin of the σ_i-space with the cylindrical surface of Eq. A26 gives the yield circle

$$\Sigma s_i^2 = \frac{2}{3}(Y^0)^2 \ . \tag{A28}$$

If the stress given by Eq. A27 is outside of the yield circle, then plastic deformation will have taken place and each of the stress deviators is reduced by the factor

$$\sqrt{(2/3)/\Sigma s_i^2}\ Y^0 \ .$$

As a result, the plastic strain component, which is perpendicular to the yield circle, is constrained to the yield circle.

Hence, for plastic flow the stress deviators have been computed, but the total stresses as given by Eq. A27 are not valid. The total stresses are computed from the simultaneous solution of an energy equation and an equation of state. For axisymmetry in the cylindrical coordinate system,

$$\dot{e} = -P\dot{v} + v(s_r\dot{\epsilon}_r + s_\theta\dot{\epsilon}_\theta + s_z\dot{\epsilon}_z + \sigma_{rz}\dot{\epsilon}_{rz}), \tag{A29}$$

where s_r and s_θ are the known stress deviators in the radial and tangential directions, and σ_{rz} is the shear stress (linearly proportional to the shear strain):

$$\dot{\sigma}_{rz} = \mu\dot{\epsilon}_{rz} + \delta_{rz} \ . \tag{A30}$$

The δ-term is a correction for the rotation of the mass element during the finite time step of the computation. The strain rates are

$$\dot{\epsilon}_r = \partial u/\partial r; \quad \dot{\epsilon}_z = \partial w/\partial z; \quad \dot{\epsilon}_\theta = u/r \ . \tag{A31}$$

The stress P is the sum of the hydrostatic pressure p and artificial viscosity q. The energy Eq. A29 together with a thermodynamic equation of state can be solved for p and e. Since the stress deviators and the hydrostatic pressures are now known, the total stress can be computed from Eq. A14, expressed in the cylindrical coordinates. From the resulting stress distribution, the computation is repeated for the next time step, which begins with the computation of the particle accelerations from the momentum equation in the cylindrical coordinate system:

$$\left.\begin{aligned} \rho\dot{u} &= -\frac{\partial(P - s_r)}{\partial r} + \frac{\partial \sigma_{rz}}{\partial r} + \frac{2s_r + s_z}{r} \; ; \\ \rho\dot{w} &= -\frac{\partial(P - s_z)}{\partial z} + \frac{\partial \sigma_{rz}}{\partial r} + \frac{\sigma_{rz}}{r} \; . \end{aligned}\right\} \tag{A32}$$

Work hardening can be introduced into the above procedure by making the yield constant Y^0 in Eq. A26 a function of the strain energy. When sufficient work has been done to melt the material, the yield constant can be set to zero, and the purely hydrodynamic case will apply, since all stress deviators will become zero and only the hydrostatic pressure p will remain.

APPENDIX B

Detonation of the Explosive Charge

The detonation of an explosive charge involves an extremely complex series of physical and chemical processes occurring on a microsecond time scale. If it were necessary to supply all details of the processes as input to the REXCO-H code, a separate large-scale computer program would be required for the detonation process alone. Fortunately, the pressure waves generated in the main bulk of the region surrounding the charge, as well as the intensity of the pressures experienced at the walls of the containment vessel, are relatively insensitive to the finer details of the detonation process. This insensitivity was demonstrated by a number of computer runs under different assumptions for the detonation process. Essentially, all that is required to produce reasonably consistent results is the proper energy input and a satisfactor equation of state for the products of the detonation.

For the purposes of the REXCO-H code the detonation process can be adequately described by analogy to the classical hydrodynamic theory of shock waves, involving only mechanical terms without reference to details of the chemical processes. The chemical reaction is assumed to take place in a narrow zone propagating at constant velocity through the explosive. The detonation process is thus treated as a shock wave, or steady discontinuous wave, governed by the conservation equations for mass, momentum, and energy. The detonation front, assumed to be a locally plane surface of discontinuity, shown in Fig. B1, advances at constant velocity U into the

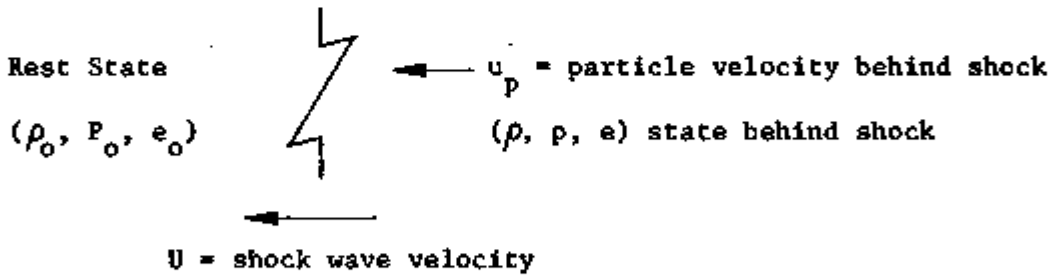

Fig. B1. Detonation Wave Advancing into Medium at Rest

unburnt region, transforming the explosive into gaseous detonation products. These gases must be described by a suitable equation of state involving the density ρ, pressure p, and internal energy e:

$$p = f(\rho, e). \qquad \text{(B1)}$$

The unsteady state shown in Fig. B1 can be easily made time-independent by considering the flow equations relative to a reference frame moving with the detonation wave, as shown in Fig. B2. The conservation equations for mass, momentum, and energy in this steady-state frame are the Rankine-Hugoniot conditions (q = chemical heat release):

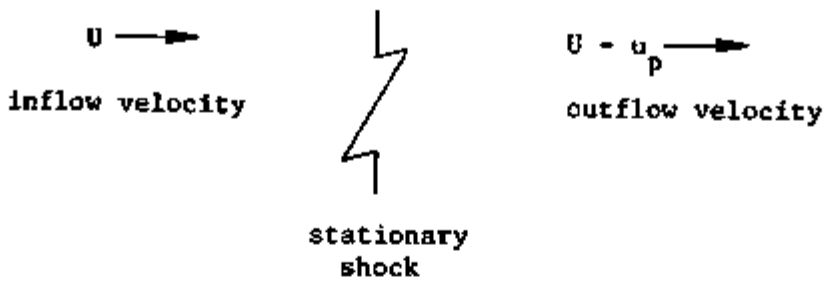

Fig. B2. Reference Frame Fixed to the Detonation Wave (Steady-state Condition)

$$\rho_o U = \rho(U - u_p) = m \; ; \tag{B2}$$

$$p - p_o = m u_p \; ; \tag{B3}$$

$$p u_p = m[(u_p^2/2) + e - e_o] - q \; . \tag{B4}$$

Elimination of the velocities from these three equations yields the Hugoniot relationship between the thermodynamic variables alone:*

$$h - h_o = \frac{1}{2}\left(\frac{1}{\rho_o} + \frac{1}{\rho}\right)(p - p_o) + q \; , \tag{B5}$$

where the enthalpy $h = e + (p/\rho)$. In terms of temperatures, the enthalpy increase is

$$h - h_o = c_p(T - T_o) \; , \tag{B6}$$

where c_p is the specific heat at constant pressure of the detonation products.

It is convenient to introduce the dimensionless variables**

$$P = p/p_o; \quad V = \rho_o/\rho; \quad \alpha = q/(p_o/\rho_o); \quad \mu = m^2/p_o \rho_o.$$

If the material is treated as a perfect gas, then Eq. B6 becomes

$$e - e_o = \frac{1}{\gamma - 1}\left(\frac{p}{\rho} - \frac{p_o}{\rho_o}\right), \tag{B7}$$

and this equation, together with Eq. B5, yields the dimensionless Hugoniot relation

---

* Or, alternatively, $e - e_o = \frac{1}{2}\left(\frac{1}{\rho_o} - \frac{1}{\rho}\right)(p + p_o) + q$.

** See, for example, F. A. Williams, *Combustion Theory*, Addison-Wesley Publishing Co., Inc., Reading, Mass. (1965), for derivations and discussions of equations (B8) - (B11).

$$P = \frac{2\alpha + \frac{\gamma + 1}{\gamma - 1} - V}{\frac{\gamma + 1}{\gamma - 1} V - 1} , \tag{B8}$$

where γ is the ratio of specific heats (constant pressure to constant volume). In the (P,V) plane, for a given mass flow μ, the locus of possible points satisfying the mass- and momentum-conservation equations is a straight line of negative slope, the Rayleigh line, shown in Fig. B3:

$$P - 1 = \mu(V - 1) . \tag{B9}$$

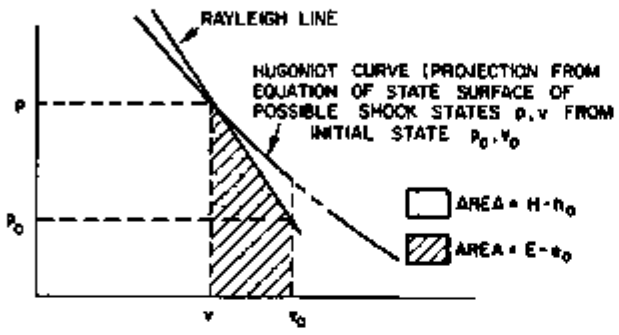

Fig. B3. The Enthalpy h and Internal Energy e Increase Across a Shock, Where E = e - q and H = h - q Are the Effective Internal Energy and Enthalpy of the Detonation Products.

Points satisfying Eqs. B8 and B9 are possible detonation states. In general, the intersection of the Rayleigh line with the Hugoniot curve will provide two such solutions, but at the point of tangency the two points converge to a single point. This solution, the Chapman-Jouguet point, is considered to describe a stable detonation front, and the corresponding Chapman-Jouguet wave at this point is assumed to be the detonation wave of constant velocity U. It is easily shown that at the Chapman-Jouguet point

$$P_c = 1 + \alpha(\gamma - 1)\left(1 + \sqrt{1 + \frac{2\gamma}{\alpha(\gamma^2 - 1)}}\right) \tag{B10}$$

and

$$V_c = 1 + \alpha\frac{\gamma - 1}{\gamma}\left(1 - \sqrt{1 + \frac{2\gamma}{\alpha(\gamma^2 - 1)}}\right) . \tag{B11}$$

At this point the entropy is a minimum, and the detonation speed is exactly the sum of the particle velocity and the local speed of sound:

$$U_c = u_p + a_c .$$

This is the basic idea of the stability of the Chapman-Jouguet wave, since small perturbations travel at the speed of sound relative to the particles and cannot penetrate the reaction zone.

It may be noted in Fig. B3 that the Hugoniot curve is divided into an upper and lower branch by a dotted portion. This dotted portion represents physically impossible states where an increase in pressure is associated with an expansion of the explosion. The detonation velocity cannot have real values since

$$U = v_o\sqrt{(p - p_o)/(v_o - v)}.$$

The lower branch is of some interest since it represents the slow-burning deflagration processes characteristic of such propellant-type explosives as gunpowder. The burning velocity in gunpowder is about 10 cm/sec, slower by a factor of 104 than for TNT. Deflagrations are millisecond phenomena compared to the microsecond time scale for detonations. The treatment of deflagrations by the hydrodynamic shock-wave analogy is not very satisfactory, because the detonation products are not compressed, but expand and flow away from the front.

As mentioned above, for the bare charge in water, the REXCO-H code was run under several different assumed detonation conditions, and no significant differences occurred in the resulting pressure distributions in the surrounding water. The first computer runs were made for the detonation products described by a "constant β" equation of state (see Amsden[10]):

$$p = (\rho e/\beta) + c_1\left[1 - \frac{1}{\beta(\gamma - 1)}\right]\rho^{\gamma} \qquad \text{(B12)}$$

where

$$\beta = 1.774; \quad \gamma = 2.769.$$

The initial density of the charge is

$$\rho_o = 1.714 \text{ gm/cm}^3,$$

and the chemical heat released in the detonation process is

$$q = 4.789(10^{10}) \text{ erg/gm}.$$

It is of interest to examine this equation of state in terms of the hydrodynamic theory of detonation outlined above. For the values given by Amsden, the energy-release parameter is

$$\alpha = q/(p_o/\rho_o) = 82{,}083 ,$$

so that

$$P_c = 290{,}413, \; V_c = 0.73465,$$

and the Chapman-Jouguet pressure and density are

$$P_c = P_c\, p_o = 290.413 \text{ kb}; \quad \rho_c = \rho_o/V_c = 2.333 \text{ gm/cm}^3.$$

The point on the Hugoniot curve where $\rho = \rho_o$ can be thought of as a limiting point, where from Eq. B2 the particle velocity is zero ($u_p = 0$). At this point, $V = 1$, and

$$P_{H,o} = \frac{2\alpha + \frac{\gamma + 1}{\gamma - 1} - 1}{\frac{\gamma + 1}{\gamma - 1} - 1} = 145{,}206;$$

the pressure at this point is

$$P_{H,o} = P_{H,o}\, p_o = 145.206 \text{ kb}.$$

The internal energy at this point can be found from Eq. B5:

$$\frac{P_{H,o}}{\rho_o} + e_{H,o} = \frac{p_o}{\rho_o} + e_o + \frac{1}{\rho_o}\ (p_{H,o} - p_o) + q,$$

so that

$$e_{H,o} = e_o + q. \tag{B13}$$

For an assumed isentropic curve through the Chapman-Jouguet point,

$$p_i/\rho^\gamma = p_c/\rho_c{}^\gamma = c \tag{B14}$$

$$= 2.782(10^{10})(\text{dyne/cm}^2)(\text{gm/cm}^3)^{-\gamma}.$$

The subscript i refers to the isentropic curve at density ρ. The internal energy on the isentropic curve is obtained by integration of the differential thermodynamic relation

$$de = T\, ds - p\, d(1/\rho).$$

For constant entropy s, the integration yields

$$e_i - e_c = \frac{1}{\gamma - 1}\left(\frac{p_i}{\rho} - \frac{p_c}{\rho_c}\right). \tag{B15}$$

Nothing has yet been said regarding the reference level for the internal energy. If the reference level is chosen so that

$$e_c = \frac{1}{\gamma - 1}\ \frac{p_c}{\rho_c} = 7.038(10^{10}) \text{ erg/gm},$$

then,

$$e_i = \frac{1}{\gamma - 1} \frac{P_i}{\rho} \quad . \tag{B17}$$

At the initial density ρ_o, the internal energy on the isentropic curve is

$$e_{i,o} = \frac{1}{\gamma - 1} \frac{P_{i,o}}{\rho_o} = 4.079(10^{10}) \text{ erg/gm}$$

and the pressure is

$$p_{i,o} = c\, \rho_o \gamma = 123.6 \text{ kb.}$$

The value of e_o (with respect to the Chapman-Jouguet point) is obtained from Eqs. B7 and B16:

$$e_o = \frac{1}{\gamma - 1} \frac{P_o}{\rho_o} = 0.33(10^6) \tag{B18}$$

$$= 0 \text{ (compared to q).}$$

The properties of the detonation wave can be summarized in Fig. B4.

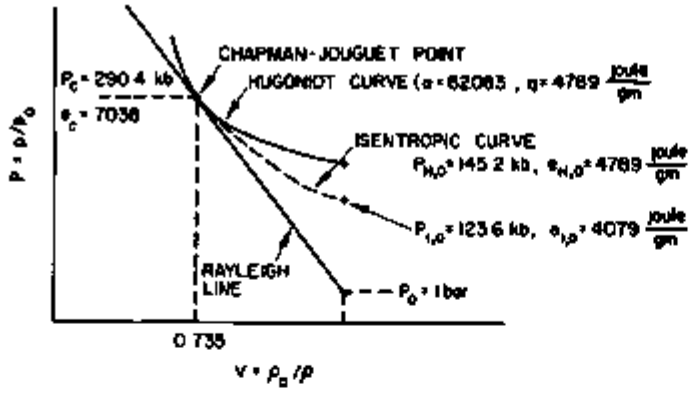

Fig. B4.
The Detonation States in the (P,V) Plane

For the Chapman-Jouguet wave, the burning velocity is derived from the Mach number

$$M_c = \sqrt{1 + \frac{\alpha(\gamma^2 - 1)}{2\gamma}} + \sqrt{\frac{\alpha(\gamma^2 - 1)}{2\gamma}} \tag{B19}$$

$$= 628.72.$$

The sonic speed in the undisturbed medium is

$$a_o = \sqrt{\gamma p_o/\rho_o} = 1271 \text{ cm/sec},$$

and consequently the burning velocity is

$$U = a_o M_c = 7991 \text{ m/sec}.$$

The particle velocity behind the detonation front is obtained from Eqs. B2 and B3:

$$u_p = (p_c - p_o)/\rho_o U = 2120 \text{ m/sec}.$$

Also, the sound speed in the detonated region is

$$a_c = \sqrt{\gamma p_c/\rho_c} = 5871 \text{ m/sec}.$$

By comparison, the values given by Dasgupta and Penney* are

$$a = 5660 \text{ m/sec}; \quad u_p = 1620 \text{ m/sec}; \quad p = 177 \text{ kb},$$

and are based upon an experimental burning velocity U of 7280 m/sec.

A Mie-Grüneisen form for the equation of state of the detonation products in the neighborhood of the isentropic curve through the Chapman-Jouguet point is

$$p = p_i + \Gamma\rho(e - e_i). \tag{B20}$$

Substitution of the values for p_i and e_i from Eqs. B14 and B17 gives exactly the "constant β" Eq. B1, where

$$\beta = 1/\Gamma; \quad c_1 = c.$$

Since conditions on both the isentropic and the Hugoniot curves are known, the value of Γ as a function of ρ can be computed:

$$\Gamma = \frac{1}{\rho}\,\frac{p_H - p_i}{e_H - e_i}.$$

However, a constant value of Γ is assumed to apply in the equation of state B1 for the products of detonation.

---

* R. H. Cole, *Underwater Explosions*, Princeton U. Press (1948), p. 100.

For the finite-difference computation in REXCO-H, a cell width is much larger than the detonation zone, which in fact is simply assumed to be a shock discontinuity ("infinitely thin"). A question is immediately raised concerning what state should be assigned to the cell containing the detonation to represent the net effect of the detonation traversing the cell. For example, suppose the entire explosive charge is contained within a single cell. The most direct method is to assume the detonation wave has passed through the cell, raising the pressure and providing the initial conditions for the REXCO-H code. The cell has not yet expanded, so the average density is still ρ_o and the average particle velocity u_p is zero. The internal energy should then be given by Eq. B13, which from Eq. B18 is essentially the chemical energy release q. Substitution of. this value for the energy into the equation of state B1 for the detonation products gives the initial pressure

$$p_o' = \rho_o(q/\beta) + c\rho_o^{\gamma}\left[1 - \frac{1}{\beta(\gamma - 1)}\right] \qquad \text{(B21)}$$

$$= 130.5 \text{ kb.}$$

This pressure differs from the 145.2-kb value shown on the Hugoniot curve (Fig. B4) because the value of Γ is assumed to be an effectively constant value in the neighborhood of the entire isentropic curve, rather than varying as a function of ρ. The selection of the value of Γ is based upon experimental measurements.

It was kindly pointed out, in a personal communication, by N. E. Hoskin, United Kingdom Atomic Energy Authority, Atomic Weapons Research Establishment, that the equation discussed above is for Grade A Composition B (64/35/1 RDX/TNT/wax by weight), and the detonation process in this explosive may differ significantly from that for the Composition B (60/40 RDX/TNT) used in the experiments. The reason for the possible difference is that the detonation velocity depends upon the percentage of RDX and the density, as shown by Deal.[12] Consequently, a more appropriate equation of state recommended by Hoskin was used to describe the detonation process in the REXCO-H code, and the results presented in Sect. III are based upon this equation:

$$P = \frac{e}{\beta_2 V} + \beta_1 \frac{(V^{1-\gamma} - 1)}{V}, \qquad \text{(B22)}$$

where

$\beta_1 = 7.511(10^{10})$ dyne/cm^2;

$\beta_2 = 1.761$ cm^3/gm;

$\rho_o = 1.67$ gm/cm^3;

$\gamma = 2.802$;

$V = \rho_o/\rho$.

That no significant differences appeared between the results computed for this equation, and the Amsden* equation, B12, is attributed by Hoskin to the fact that the energy release is less dependent upon the percentage of RDX than is the detonation velocity. For comparison of the two equations reference should be made to Skidmore[11] (p. 250), where the modification of the constant-β equation by Pike for pressures down to the order of 1 kb yields Eq. B22.

It is of interest to compare Eqs. B12 and B22 in terms of the discussion leading to Fig. B4. If in Eq. B22 the initial pressure is taken to be $p_o = 0$ (i.e., "gauge pressure" rather than absolute pressure) at the initial density $\rho = \rho_o$ (i.e., $V = 1$), then the corresponding initial energy reference level is $e_o = 0$. The energy reference level for the Amsden Eq. B12 can be shifted to correspond to this condition:

$$p = \frac{\rho}{\beta}(e - e_{ref}) + c\left[1 - \frac{1}{\beta(\gamma - 1)}\right]\rho^{\gamma} . \qquad (B23)$$

It follows that

$$e_{ref} = \beta c\left[1 - \frac{1}{\beta(\gamma - 1)}\right]\rho_o^{\gamma-1}$$

and

$$p = \frac{e}{(\beta/\rho_o)V} + c\left[1 - \frac{1}{\beta(\gamma - 1)}\right]\rho_o^{\gamma}\frac{V^{1-\gamma} - 1}{V} . \qquad (B24)$$

Thus, the Amsden Eq. B12 is transformed to the same form as the Hoskin Eq. B22 by a simple shifting of the initial e_o energy reference level, where

$$\beta_2 = \beta/\rho_o; \quad \beta_1 = c\left[1 - \frac{1}{\beta(\gamma - 1)}\right]\rho_o^{\gamma}.$$

We are now in a position to compare the parameters for the two explosives (in terms of form B12).

Property	Comp B (Eq. B22) (60/40 RDX/TNT)	Grade A Comp B (Eq. B12) (64/35/1 RDX/TNT/wax)
ρ_o, gm/cm^3	1.67	1.714
β	2.941	1.774
c, $\frac{\text{dyne/cm}^2}{(\text{gm/cm}^3)^{\gamma}}$	2.200 (10^{10})	2.782 (10^{10})
γ	2.802	2.769
p_o', kb	102.3	130.5

* Actually, the constant-β equation of state is attributed to W. E. Deal, *Third Symposium on Detonation*, ONR Symposium Report, ACR-52, Vol. 2, p. 386 (1960).

The value of p_o' is obtained by transforming back from the Hoskin (or Pike) form to the Amsden (or Deal) form, and substituting the new values of ρ_o, B, c, and γ for the same chemical energy release q.

At the interface between the explosive charge and the water, the pressure transferred to the water must satisfy a wave diagram matching the pressure and particle velocities on either side of the interface. Since the impedance of the water is less than that of the explosive, a reflected rarefaction will travel back into the explosive. If we assume that the detonation and rarefaction waves are of equal strength, since the entropy change through the shock is of third order in shock strength, the reflected rarefaction is the mirror image about the line of symmetry, as shown in Fig. B5. Based upon values given in Ref. 9, the intersection of this reflected curve with the water shock-wave Hugoniot (in the p, u_p plane) gives an interface pressure of 103 kb.*

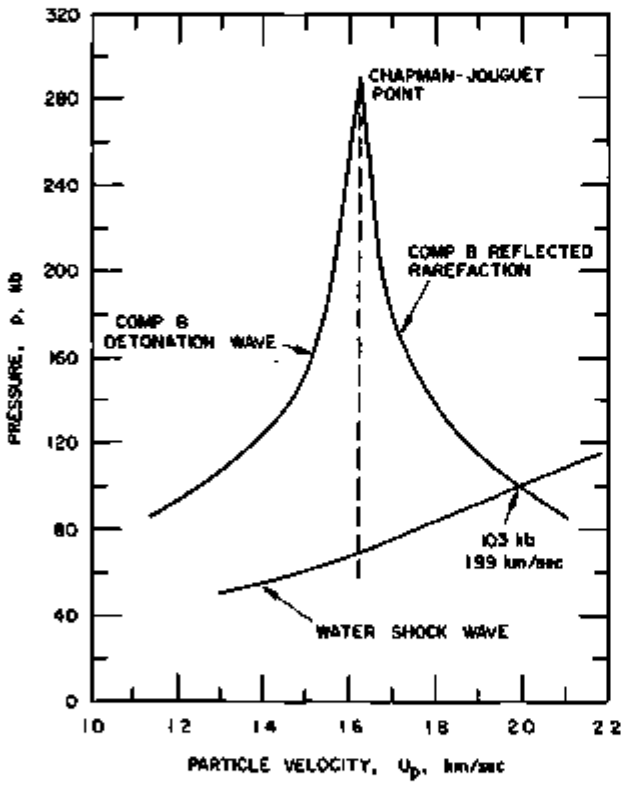

Fig. B5. Determination of the Interface State (Values from M. van Thiel et al.[9]).

For the given heat release [q = 4.789(10^{10}) erg/gm] and specified γ = 2.802, the Chapman-Jouguet pressure for the explosive with an initial density ρ_o = 1.67 gm/cm^3 can be computed from Eq. B10, and the Chapman-Jouguet density from Eq. B1:

$$p_c = 288.2 \text{ kb}; \quad \rho_c = 2.266 \text{ gm/cm}^3.$$

---

* Hoskin has indicated that the value of 103 kb is too low; an exact one-dimensional solution of the shock interaction yielded a value of 183 kb.

The corresponding detonation velocity is computed by means of Eq. B19 for a sonic speed a_o = 1295 cm/sec:

$$U = 8100 \text{ m/sec.}$$

The pressure on the Hugoniot curve at V = 1 is computed from Eq. B8:

$$p_{H,o} = 160 \text{ kb} .$$

For the isentropic curve through the Chapman-Jouguet point the value of c is given by Eq. B14, yielding the corresponding pressure on the isentropic curve at V = 1:

$$c = 2.913(10^{10}) \text{ (dyne/cm}^2\text{) (gm/cm}^3\text{)}^{-\gamma};$$

$$p_{i,o} = 123 \text{ kb.}$$

For this value of c and the value β = 2.941, the pressure given by Eq. B21 is

$$p_o' = 180 \text{ kb} .$$

The REXCO-H computation was initialized in several different ways. The first and most simple method was to assume that the detonation wave has passed through the charge before any significant expansion of the charge has taken place. The net effect is to raise the pressure to p_o' while the average charge-particle velocity is zero. The REXCO-H computation was performed for both the Amsden equation of state with an initial p_o' = 130.5 kb and the Hoskin equation of state, both for the same chemical energy release of $q = 4.789(10^{10})$ erg/gm. In both cases the pressure in the surrounding water quickly adjusted to very nearly the same distribution. Also, the initial charge pressure, density, and particle velocity distributions computed by Dasgupta and Penney (cited above) were introduced as initial conditions into the REXCO-H code. Again, no significant changes resulted in the computed pressure distribution in the surrounding water.

The method finally adopted for computing the detonation was the "constant-burning process." This method is perhaps the most realistic description of the actual physical process, although the end result differs little from the above-mentioned initial conditions. Constant burning is a simple process whereby for each time cycle of the computation the energy of the burned portion in each cell is added to the cell energy, and the resulting pressure increase of the cell is computed from the simultaneous solution of the equation of state and energy equation. In this way the pressure in the cell builds up in time from zero to some final value when the explosive in the cell is completely burned.

APPENDIX C

The Artificial Viscosity

1. The Scalar Artificial Viscosity

The scalar artificial viscosity introduced by von Neumann and Richtmyer* to avoid the problems of shock fitting for one-dimensional problems was of the form

$$q = \frac{\ell^2}{v}\left(\frac{\partial u}{\partial R}\right)^2 .$$

This stress term is taken to be zero for expansions. An equivalent form for one-dimensional plane flow is

$$q = \frac{(\rho_o \ell)}{v}(\dot{v})^2 .$$

For cylindrical flows the two forms are not equivalent, and ℓ^2 is replaced by aA_oR/r, where 'a' is a shock width constant and A_o is the original Lagrangian mesh area at initial density ρ_o:

$$q = \frac{a^2\rho_o A}{v^2}(\dot{v})^2 . \qquad (C1)$$

The area A is the deformed mesh area at time t and density ρ. The value of v is negative (for compression); otherwise, q is zero, and for REXCO-H the value of 'a' is taken to be 1.2. Larger values of 'a' will spread the shock width out more.

The artificial stress q is added to the hydrostatic pressure p, and an effective pressure $P = p + q$ replaces the pressure p in the momentum and energy equations

$$\rho\dot{\bar{u}} = -\nabla P \qquad (C2)$$

and

$$\dot{e} = -P\dot{v} . \qquad (C3)$$

---

* R. D. Richtmyer and K. W. Morton, *Difference Methods for Initial-Value Problems*, Interscience Publishers, New York (1967).

The REXCO-H computation proceeds as follows:

i. For the initial pressure, velocity, and density distribution, accelerations are computed from Eq. (C2).

ii. For the specified time step, incremental velocities and the resulting new velocity distribution are computed.

iii. From the new velocity distribution, displacements and cell sizes are computed, and from mass conservation, the new cell densities are determined ($\rho_j^i = M_j^i/\tau_j^i$ for the (i,j) cell, the fixed cell mass divided by the new cell volume).

iv. The new pressure and internal energy are computed from the simultaneous solution of the energy and state equations:

$$e_{t+\Delta t} = e_t - \frac{1}{2}(P_t + P_{t+\Delta t})\ \Delta v \ ;$$

$$P_{t+\Delta t} = f(v_{t+\Delta t},\ e_{t+\Delta t}) \ ;$$

$$q_{t+\Delta t} = a^2 \rho_o A_{t+\Delta t} \frac{1}{v_{t+\Delta t}} \left(\frac{\Delta v}{\Delta t}\right)^2$$

$$= 0 \text{ for } \frac{\Delta v}{\Delta t} > 0 \ .$$

Under certain special circumstances the use of an artificial viscosity as described above may lead to instabilities at certain cells. An example of such an instability was described in Appendix A, Sect. 3. Various modifications may be introduced which will avoid some of the possible difficulties. However, it should be recognized that a price must be paid by using a more complicated q-term. Instabilities may still occur, and additional complications will usually make the problem of tracking down the cause of the instability more difficult.

One obvious means of reducing the tendency towards an instability at a particular cell is effectively to spread out the influence of q. The instability discussed in Appendix A, Sect. 3 was due to a strong relationship between the e and p values in the cell to the q value. This relationship can be weakened if, rather than using a simple q-value for a cell, the values surrounding the cell are used. This can easily be accomplished by changing the finite-difference equations. The finite-difference approximation to a given differential equation is not unique. The form of the energy equation (C3) can be changed by using the continuity equation

$$\dot{v} = v\ \nabla \cdot \bar{u} \ . \qquad \text{(C4)}$$

The energy equation can then be expressed as

$$\rho \dot{e} = -P \nabla \cdot \bar{u} .$$

Combining with the momentum equation C2 yields*

$$\rho \frac{D}{Dt} \left(e + \frac{1}{2} \bar{u} \cdot \bar{u}\right) = -\nabla \cdot P\bar{u} . \tag{C5}$$

For cylindrical coordinates and axial symmetry this form becomes

$$e = -p \left(\frac{1}{r} \frac{\partial ur}{\partial r} + \frac{\partial w}{\partial r}\right) \cdot \frac{1}{r} \frac{\partial qur}{\partial r} - \frac{\partial qw}{\partial z} + u \frac{\partial q}{\partial r} + w \frac{\partial q}{\partial z} . \tag{C6}$$

The corresponding finite-difference form for the right-hand side of this equation involves a single pressure for the cell, but q will enter in terms of differences across the cell:

$$(\partial q/\partial r)^i_j = \left(q^{i+1}_j - q^{i-1}_j\right) \Big/ 2\Delta r;$$

$$(\partial q/\partial z)^i_j = \left(q^i_{j+1} - q^i_{j-1}\right) \Big/ 2\Delta z.$$

Although the gradient is directional, q is a scalar for each cell. The value of q itself can be given a directional property by using an alternative form based upon the divergence of the velocity vector:

$$q_R = a^2 \rho A_o \frac{R}{r} \left(\frac{\partial u}{\partial R}\right)^2 \quad \text{for the radial gradient component}$$

$$q_z = a^2 \rho A_o \frac{R}{r} \left(\frac{\partial w}{\partial z}\right)^2 \quad \text{for the axial gradient component} \tag{C7}$$

The application of such a directional artificial viscosity is discussed

---

* The dot over the symbol is equivalent to D/Dt, both indicating the time derivative along the particle path (i.e., holding the Lagrangian coordinate fixed).

by Schultz.* The physical interpretation of this directional viscosity presented below is based upon his article.

2. A Directional Artificial Viscosity

Suppose the shock front is resolved into two orthogonal components in the Lagrangian (R,Z) space, as shown in Fig. C1. The transformation to Eulerian coordinates is not conformal, so in the (r,z) space the two shock-front components do not remain orthogonal.

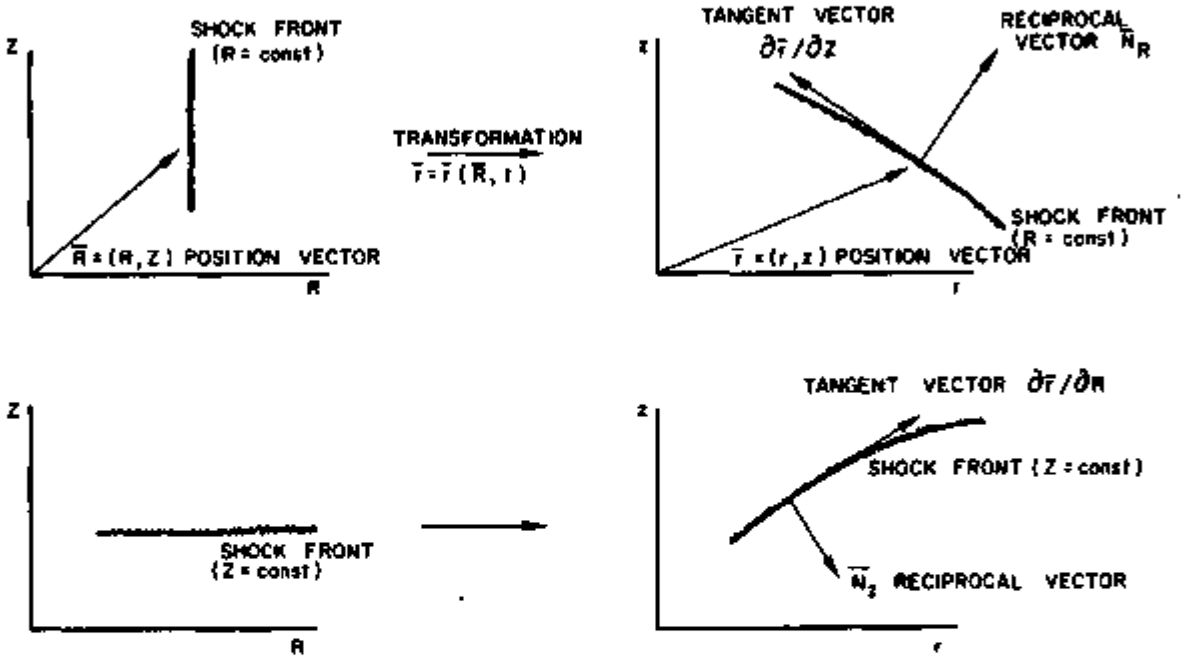

Fig. C1. Resolution of the Shock Front into the Lagrangian R and Z Directions

The momentum equation C2 is

$$\rho \dot{\bar{u}} + \nabla p = -\nabla q,$$

where the gradient vector operator is

$$\nabla = \left(\frac{\partial}{\partial r}, \frac{\partial}{\partial z} \right)$$

$$= \frac{r}{RJ} \left(\frac{\partial z}{\partial Z} \frac{\partial}{\partial R} - \frac{\partial z}{\partial R} \frac{\partial}{\partial Z}, - \frac{\partial r}{\partial Z} \frac{\partial}{\partial R} + \frac{\partial r}{\partial R} \frac{\partial}{\partial Z} \right).$$

---

* W. D. Schultz, "Two-dimensional Difference Equations" in *Methods in Computational Physics*, Academic Press (1964).

Now the reciprocal vectors, or normal vectors, to the tangents $\partial\bar{r}/\partial Z$ and $\partial\bar{r}/\partial R$ are

$$\bar{N}_Z = \left(\frac{\partial z}{\partial R}, -\frac{\partial r}{\partial R}\right); \quad \bar{N}_R = \left(\frac{\partial z}{\partial Z}, -\frac{\partial r}{\partial R}\right).$$

Hence, the momentum equation becomes

$$\rho\dot{\bar{u}} + \nabla p = -\frac{r}{RJ}\left(\bar{N}_R \frac{\partial q}{\partial R} - N_Z \frac{\partial q}{\partial Z}\right).$$

Since $\bar{N}_R$ is in the direction of motion of the constant-R shock front, the artificial viscosity for this direction, q_R, may be considered to have a different value from the artificial viscosity q_Z in the $\bar{N}_Z$ direction, i.e., the artificial viscosity can be regarded by direct extension to be a vector quantity

$$\bar{q} = (q_R, q_Z), \tag{C8}$$

and

$$\rho\dot{\bar{u}} + \nabla p = -\frac{r}{RJ}\left(\bar{N}_R \frac{\partial q_R}{\partial R} - \bar{N}_Z \frac{\partial q_Z}{\partial Z}\right)$$

$$= -\left(\frac{\partial q_R}{\partial r} + \frac{\partial q_Z}{\partial z}\right)$$

or

$$\rho\dot{\bar{u}} + Dp = -D\cdot\bar{q},$$

when the vector operator D is defined to have the properties

$$\left.\begin{aligned} Dp &= \nabla p; \\ D\cdot\bar{q} &= \nabla\cdot\bar{q} - \frac{q_R}{r} \end{aligned}\right\}. \tag{C9}$$

The energy equation will be of the same form as Eq. A29 when the stress deviators are analogous to the artificial viscous stresses q_R and q_Z:

$$\dot{e} + p\dot{v} = -\frac{r}{RJ} v \left(q_R \bar{N}_R \cdot \frac{\partial \bar{u}}{\partial R} - q_Z \bar{N}_Z \cdot \frac{\partial \bar{u}}{\partial Z}\right). \tag{C10}$$

The effective velocity gradient in the R and Z directions will be designated by

$$\left(\frac{\partial \bar{u}}{\partial R}\right)_R = \bar{e}_R \cdot \frac{\partial \bar{u}}{\partial R} \; ; \quad \left(\frac{\partial \bar{u}}{\partial Z}\right)_Z = \bar{e}_Z \cdot \frac{\partial \bar{u}}{\partial Z} \; ,$$

when $\bar{e}_R$ and $\bar{e}_Z$ are the unit normal vectors

$$\bar{e}_R = \bar{N}_R/|\bar{N}_R| ; \quad \bar{e}_Z = \bar{N}_Z/|\bar{N}_Z| \; .$$

The viscosities will then be

$$\left.\begin{aligned} q_R &= a^2 \rho A_o \frac{R}{r} \left(\frac{\partial \bar{u}}{\partial R}\right)_R^2 \; ; \\ q_Z &= a^2 \rho A_o \frac{R}{r} \left(\frac{\partial \bar{u}}{\partial Z}\right)_Z^2 \end{aligned}\right\} \; . \tag{C11}$$

For a uniform expansion or contraction over the entire medium the derivative of the velocity gradient would be zero. It would be desired that the artificial viscosity be independent of such a condition, so Schultz expresses the viscosity by the form

$$\left.\begin{aligned} q_R &= -\rho \ell^2 \left(\frac{\partial \bar{u}}{\partial R}\right)_R \left| \frac{\partial}{\partial R} \left(\frac{\partial \bar{u}}{\partial R}\right)_R \right| \; ; \\ q_Z &= -\rho \ell^2 \left(\frac{\partial \bar{u}}{\partial Z}\right)_Z \left| \frac{\partial}{\partial R} \left(\frac{\partial \bar{u}}{\partial Z}\right)_Z \right| \end{aligned}\right\} \; . \tag{C12}$$

Schultz sets ℓ^2 equal to two, rather than to $a^2 A_o R/r$ as in Eq. C11.

APPENDIX D

The Equation of State for a Porous Material

In the configuration for the experiment shown in Fig. 2, lead shot surrounds the explosive charge to simulate the reactor breeder section. The lead shot and the porous graphite attenuated the pressure reaching the tank wall by a factor of about six, as shown in Fig. D1, and significantly altered the shape of the pressure profile behind the shock front. The void content of the lead shot and graphite is of the order

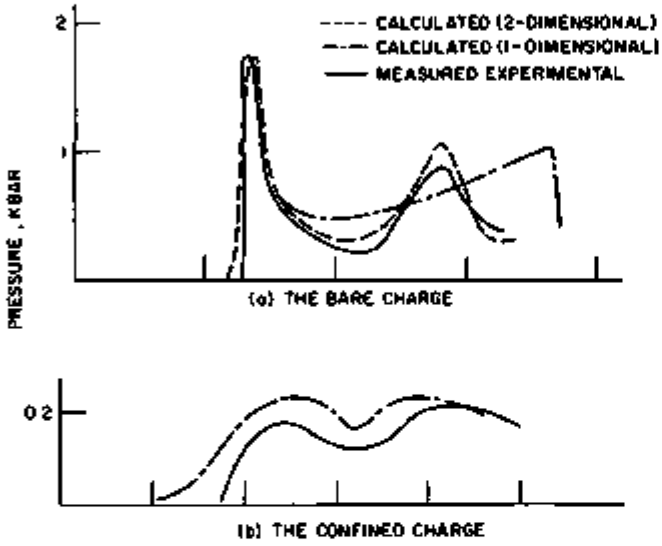

Fig. D1. Comparison of Measured Loadings vs. Time at Gauge 3 for Bare and Confined Charges[7]

of 30 to 40%, and the work required to crush the voids absorbs a large fraction of the available energy.

1. Hydrodynamic Crushing

The first computation made with REXCO-H treated the lead-shot region purely hydrodynamically, i.e., with zero shear stresses. The material in each cell was loaded up to its yield stress to overcome the initial rigidity, and then was allowed to compact at constant stress until the voids were completely closed. From that point on the Mie-Grüneisen equation of state, referred to the material Hugoniot curve, was used to describe the (p,v) relationship.

The Hugoniot for the completely compacted porous material must be above the Hugoniot for the solid because of the energy absorbed during the compaction process. This can be shown from the following considerations. (For simplicity the Hugoniot reference pressure at the yield point will be taken as zero.) The Hugoniot curves are shown in Fig. D2, where the asterisk refers to the nonporous material.

If the initial porosity of the material is α, then the initial specific volume is

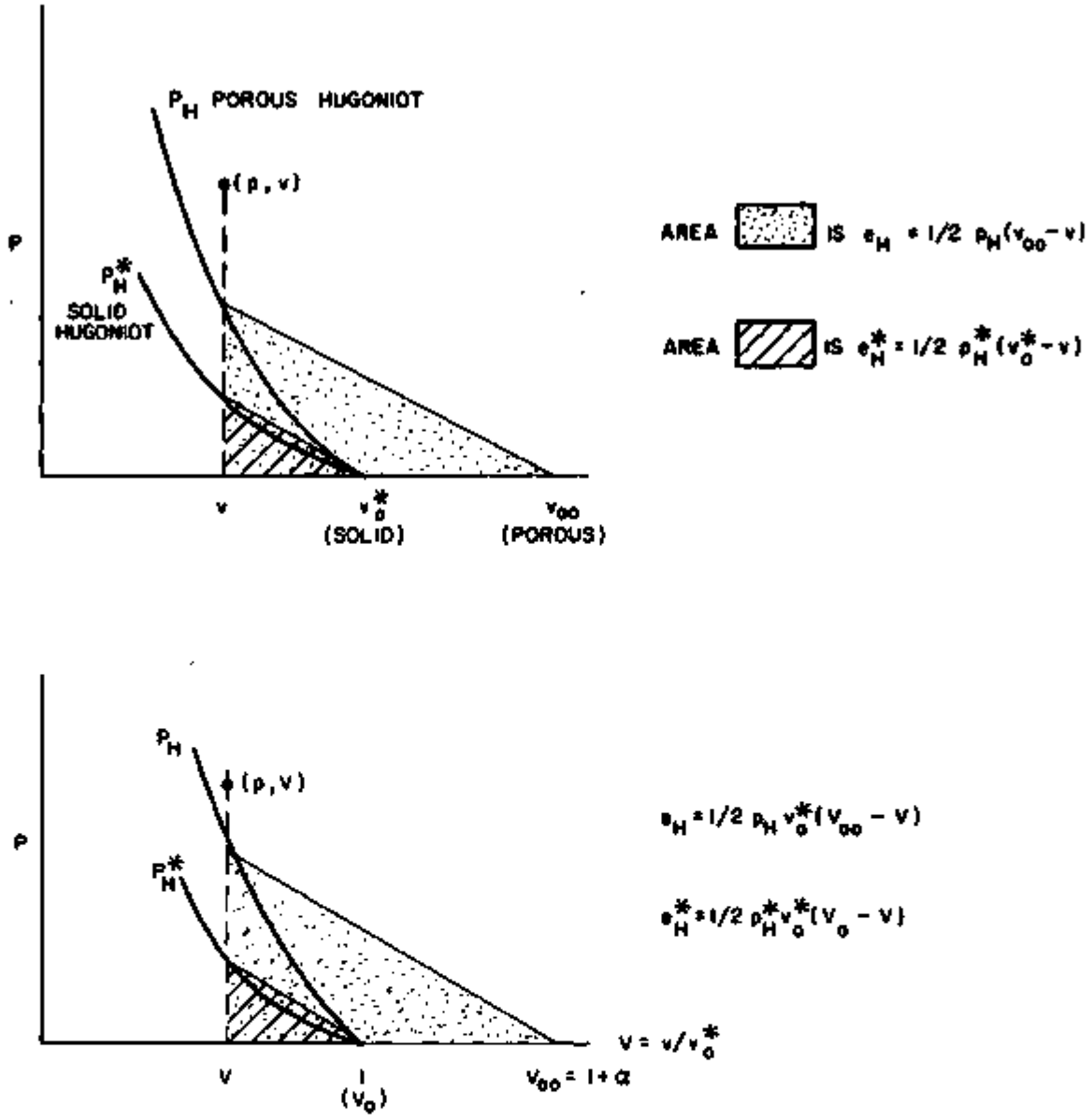

Fig. D8. The Hugoniot Curves for the Solid and Porous-material States

$$v_{oo} = (1 + \alpha)v_o^* ,$$

where v_o^* is the initial specific volume of the solid material. It is convenient to let

$$V = v/v_o^* .$$

Hence, for a material with, say, 40% voids,

$$V_{oo} = 1 + \alpha = 1.4 .$$

The pressure and internal energy relation at a given specific volume for any point off the Hugoniot is given by the Mie-Grüneisen equation with respect to the solid Hugoniot:

$$e = e_H^* + \frac{v}{\Gamma}(p - p_H^*). \tag{D1}$$

In particular, for a point on the compacted porous-material Hugoniot,

$$e_H = e_H^* + \frac{v}{\Gamma}(p_H - p_H^*). \tag{D2}$$

Substitution of this expression into Eq. D1 gives

$$e = e_H + \frac{v}{\Gamma}(p - p_H) \tag{D1'}$$

which is the Mie-Grüneisen equation with reference to the Hugoniot for the compacted porous material and is exactly equivalent to Eq. D1, i.e., either form will yield the same results.

Substitution of the values for e_H and e_H^* into Eq. D2, i.e., the triangular areas shown in Fig. D2, will give the ratio of p_H to p_H^*:

$$\frac{p_H}{p_H^*} = \frac{\left(\frac{2}{\Gamma} + 1\right) - \frac{V_o}{V}}{\left(\frac{2}{\Gamma} + 1\right) - \frac{V_{oo}}{V}} \tag{D3}$$

Since V_{oo} is greater than V_o, i.e., greater than 1, the Hugoniot p_H for the crushed material must be greater than p_H^* for the uncrushed solid material.

The slopes of the Hugoniots at V_o are proportional to the same speeds:

$$\left(\frac{C_o}{C_o^*}\right)^2 = \frac{dp_H}{dp_H^*} = \frac{\frac{2}{\Gamma}}{\frac{2}{\Gamma} - (V_{oo} - 1)} \tag{D4}$$

Since the ratio is greater than one, the sonic speed in the compacted material is greather than that in the uncrushed solid material, which, since both materials are at the same pressure and density, indicates that the compacted material is at a higher temperature.

2. Elastic-Plastic Crushing

The computed attenuation of the pressure wave based upon hydrodynamic crushing of the lead shot was not nearly enough to compare with the experimental measurements. Consequently, energy dissipation through shearing

and plastic flow was introduced through the elastic-plastic equations described in Appendix A, Sect. 5. The application of these equations in the code requires an equation of state relating the hydrostatic pressure p and the internal energy e at a given specific volume. An equation of state including elastic-plastic effects for a porous material is discussed below based upon a paper by Herrmann.*

After the material is fully compacted, the equation of state will be based upon the Hugoniot for the hydrodynamic case as discussed above. However, for the period before the material is fully compacted, it will be treated as shown in Fig. D3.

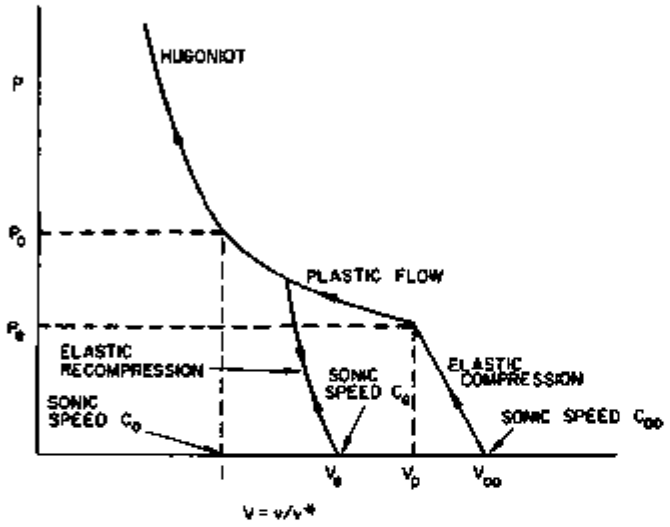

Fig. D3.
Elastic-Plastic Behavior of Porous Material before Complete Compaction.

The differential equation for the elastic compression (or recompression) curves is given by

$$\frac{dV}{dp} = V'(p) = \frac{V}{K_o^*}\left(1 - \frac{V}{h^2(V)}\right), \tag{D5}$$

where K_o^* is the bulk modulus of the solid material:

$$K_o^* = -v_o^*\left(\frac{\partial p}{\partial v^*}\right)_s = C_o^{*2}/v_o^* . \tag{D6}$$

The function h(V) can be based upon experiments; a simple form is the linear relation

$$h(V) = aV + b, \tag{D7}$$

---

* W. Herrmann, *Constitutive Equation for the Dynamic Compaction of Ductile Porous Materials*, J. Appl. Physics, *40*, 2490-2499 (1969).

where

$$a = \left(\frac{C_{oo}}{C_o^*} - 1\right) \Big/ \left(V_e - 1\right) ; \quad b = 1 - a . \tag{D8}$$

Hence, to solve Eq. D5 by finite differences for the elastic compression curve, all that need be known are the sonic speeds C_δ and C_{oo} and the elastic limits which are given by the plastic curve. The plastic curve can be represented by the quadratic form

$$\frac{V - 1}{V_p - 1} = \left(\frac{p_o - p}{p_o - p_e}\right)^2 \tag{D9}$$

The assumptions underlying the elastic-plastic curves are given by Eqs. D5 and D9 will be summarized in the following development. (The asterisk will indicate the uncrushed solid material.)

The solid material is assumed to have a thermodynamic equation of state

$$p = f(v^*, e) .$$

The sound speed is the velocity of a small isentropic compression wave:

$$C^* = - v^{*2}(\partial p/\partial v^*)_s = v^* K^* .$$

The isentropic derivative is

$$\left(\frac{\partial p}{\partial v^*}\right)_s = \frac{\partial f}{\partial v^*} + \frac{\partial f}{\partial e}\left(\frac{\partial e}{\partial v^*}\right)_s ,$$

but

$$\left(\frac{\partial p}{\partial v^*}\right)_s = -p ,$$

so that

$$\left(\frac{\partial p}{\partial v^*}\right)_s = \frac{\partial f}{\partial v^*} - p\,\frac{\partial f}{\partial e} . \tag{D10}$$

Hence, for the initial conditions $p = 0$, $v^* = v_o^*$, and $C^* = C_o^*$, it follows that

$$K_o^* = -v_o^*(\partial f/\partial v^*)_o; \quad C_o^{*2} = v_o^* K_o^* .$$

The porous material is also assumed to have a thermodynamic equation of state:

$$V = \phi(p,v) .$$

The explicit representation of the V(p) curve in Fig. D3 has the total derivative (for constant entropy)

$$V'(p) = \left(\frac{\partial \phi}{\partial v}\right)_s \left(\frac{\partial v}{\partial p}\right)_s .$$

The isentropic derivative analogous to Eq. D10 is

$$\left(\frac{\partial p}{\partial v}\right)_s = \frac{\partial f}{\partial v^*}\left(\frac{\partial v^*}{\partial v}\right)_s - p\,\frac{\partial f}{\partial e} , \tag{D11}$$

where

$$\left(\frac{\partial v^*}{\partial v}\right)_s = \frac{1}{V} - \frac{v}{V^2}\left(\frac{\partial \phi}{\partial v}\right)_s$$

$$= \frac{1}{V}\left[1 - vV'(p)\left(\frac{\partial p}{\partial v}\right)_s\right] . \tag{D12}$$

Combination of Eqs. D11 and D12 gives

$$\left(\frac{\partial p}{\partial v}\right)_s = \frac{\frac{1}{V}\,\frac{\partial f}{\partial v^*} - p\,\frac{\partial f}{\partial e}}{1 + \frac{v}{V^2}\,V'(p)\,\frac{\partial f}{\partial v^*}} . \tag{D13}$$

This equation will be considered first for the initial elastic compression from V_{oo} and then for an elastic recompression from any V_e.

For the initial elastic compression from V_{oo}, the conditions at p = 0 are $v^* = v_o^*$, $V = V_{oo} = v_{oo}/v_o^*$, so that

$$C_{oo}^2 = \frac{V_{oo}}{1 - K_o^*\,V'_{oo}\,(0)/V_{oo}}\,C_o^{*2} , \tag{D14}$$

At any other point on the axis (p = 0) the condition $V = V_e = v_e/v_o^*$ yields

$$C_e^2 = \frac{V_e}{1 - k_o^* V_e'(0)/V_e} C_o^{*2}. \tag{D15}$$

The value C_e is assumed to vary continuously from C_{oo} to C_o^*, so that

$$C_e = h(V_e)C_o^* , \tag{D16}$$

where the continuous function h must satisfy the conditions

$$\begin{cases} h(1) = 1 \\ h(V_{oo}) = C_e/C_o^* . \end{cases}$$

Combination of Eqs. D15 and D16 yields

$$V_e'(0) = \frac{V_e}{K_o}\left[1 - \frac{V_e}{h^2(V_e)}\right]. \tag{D17}$$

The relations D14 through D17 strictly hold only on the axis (p = 0), whereas if the compression is taking place along the plastic curve the pressure is not zero. If the pressure should be relieved at some point, the material is to expand along some elastic curve. To obtain the shape of this elastic curve, it will be assumed that along this curve the conditions D15 and D16 are similar:

$$C^2 = \frac{V(p)}{1 - k_o^* V'(p)/V(p)} C_o^{*2} , \tag{D18}$$

$$C = h(V)C_o^* , \tag{D19}$$

and the differential Eq. D5 is derived. The numerical finite-difference integration will then proceed down from the point on the plastic curve during the expansion. If the material is recompressed, it will proceed back up this elastic curve until it again reaches the plastic curve, which it follows for further compression.

ACKNOWLEDGMENTS

The authors wish to thank S. H. Fistedis, who initiated the Fast Reactor Containment Program at Argonne National Laboratory, for his advice and encouragement throughout the course of this work. The assistance of Y. Chang and J. Gvildys with the details of the analysis and codes incorporated into REXCO is appreciated. The cooperation and help of the other members of the Engineering Mechanics Section, Reactor Analysis and Safety Division, is also acknowledged. Finally, the authors wish to thank N. E. Hoskin of Atomic Weapons Research Establishment, UKAEA, for clarification and reassurance of the authors' interpretation of the published British Experiments used in these comparisons.

REFERENCES

1. Y. Chang, J. Gvildys, and S. H. Fistedis, *Two-dimensional Hydrodynamics Analysis for Primary Containment*, ANL-7498 (Nov. 1969).

2. N. J. M. Rees, "A Model Investigation of Explosion Containment in Single-tank Fast Reactors;" E. P. Hicks and D. C. Menzies, "Theoretical Studies on the Fast Reactor Maximum Accident;" D. E. J. Samuels, "Design Factors Influencing the Containment of Internal Explosion in Fast Reactors;" in *Proc. of the Conf. on Safety, Fuels, and Core Design in Large Fast Power Reactors*, ANL-7120 (Oct. 1965).

3. G. A. V. Drevon, M. F. G. Falgayrettes, and F. J. Walford, "Comparison of Pressure Loading Produced by Contained Explosions in Water and Sodium," *Proc. of the Conf. on Safety, Fuels, and Core Design in Large Fast Power Reactors*, ANL-7120 (Oct. 1965).

4. W. R. Wise, J. F. Proctor, and L. P. Walker, *Response of Enrico Fermi Reactor to TNT Simulated Nuclear Accidents*, NOLTR 62-207 (Nov. 1964).

5. M. L. Wilkins, "Calculation of Elastic-plastic Flow" in *Methods in Computational Physics*, Academic Press (1964).

6. G. Cinelli, J. Gvildys, and S. H. Fistedis, *Inelastic Response of Primary Reactor Containment to High-energy Excursions*, ANL-7499 (Nov. 1969).

7. N. E. Hoskin, *The Use of Computers in Investigations on Hydrodynamic Aspects of Reactor Safety Problems*, AWRE News, *17*, 16-19 (Feb. 1970).

8. M. H. Rise and J. M. Walsh, *Equation of State of Water to 250 Kilobars*, J. Chem. Phys. *26*, 824-830 (1957).

9. M. van Thiel, A. S. Kusibov, and A. C. Mitchell, *Compendium of Shock Wave Data*, UCRL-50108 (Vol. 1, Suppl. 1) (Oct. 1967).

10. A. A. Amsden, *The Particle-in-Cell Method for the Calculation of the Dynamics of Compressible Fluids*, LA-3466 (1966).

11. I. C. Skidmore, *The Physics of Detonation*, Sci. Prog. (Oxford), *55*, 239-257 (1967).

12. W. E. Deal, *Phys. Fluids*, *1*, 523 (1958).